

# Improvements of the Lateral Distribution Function of Scintillator Surface Detectors

Optimierung der lateralen Verteilungsfunktion des  
Plastik-Szintillationsdetektors

Bachelor's Thesis of

Helena Lamprecht

at the KIT Department of Physics  
Institute for Astroparticle Physics (IAP)

Reviewer:	Prof. Dr. Ralph Engel
Second Reviewer:	Dr. Markus Roth
Supervisor:	Dr. Quentin Luce

February 2022



# Erklärung zum selbstständigen Schreiben

Ich versichere wahrheitsgemäß, die Arbeit selbstständig verfasst, alle benutzten Quellen und Hilfsmittel vollständig und genau angegeben und alles kenntlich gemacht zu haben, was aus Arbeiten anderer unverändert oder mit Abänderungen entnommen wurde sowie die Satzung des KIT zur Sicherung guter wissenschaftlicher Praxis in der jeweils gültigen Fassung beachtet zu haben.

**Karlsruhe, den 25.02.2022**

---

Helena Lamprecht

---

Prof. Dr. Ralph Engel



# Abstract

The surface detector of the Pierre Auger Observatory is measuring the density of particles of extensive air showers on ground. In case of inclined air showers, an azimuthal asymmetry in the measured signals arises, due to geometrical effects and attenuation processes occurring during the shower evolution. This asymmetry introduces a bias in the reconstruction of the shower parameters, such as the position of the shower core. To correct this asymmetry in water-Cherenkov detectors, a model has already been created [1], but as part of the AugerPrime upgrade, a scintillator surface detector is installed on top of each water-Cherenkov detector.

Due to the different detector responses of the water-Cherenkov detector compared to the scintillator surface detector, different behaviors of the asymmetry are expected. To determine the impact of the asymmetry on the reconstructed observables, studies of the evolution of the azimuthal asymmetry in signals, measured with water-Cherenkov detectors and scintillator surface detectors, are conducted.

Using simulated showers, initiated by a proton primary using EPOS-LHC as hadronic model, a parametrization correcting the bias in the position of the shower core is derived for both, water-Cherenkov detectors and scintillator surface detectors. To this end, numerous model fitting processes are performed to describe the dependencies on the amplitude of the asymmetry on zenith angle and energy of the cosmic ray and on distance from the shower axis. The derived model for the water-Cherenkov detector is applied to the data and the improvements are evaluated based on the bias and resolution of the core position. The application of the derived model, corrects the bias in the position of the core to a residual bias below  $\pm 10$  m and improves the core resolution by  $\sim 20$  to 40 m.



# Zusammenfassung

Der Oberflächendetektor des Pierre Auger Observatoriums misst die Teilchendichte eines ausgedehnten Luftschauers am Erdboden. Bei einem geneigt einfallenden Luftschauer weist die laterale Teilchendichte eine azimutale Asymmetrie auf, welche auf geometrische Effekte und Dämpfungen während der Schauerentwicklung zurückzuführen sind. Diese Asymmetrie führt zu einem Bias in der rekonstruierten Position des Schauerkerns. Um den Einfluss der Asymmetrie auf die rekonstruierten Schauerparameter in Wasser-Cherenkov-Detektoren zu korrigieren, wurde bereits ein Modell entwickelt [1]. Als Teil des gerade durchgeführten AugerPrime Upgrades des Pierre Auger Observatoriums wird jedoch ein Plastik-Szintillationsdetektor auf jedem Wasser-Cherenkov-Detektor installiert.

Aufgrund der unterschiedlichen Detektorantworten des Wasser-Cherenkov-Detektors im Vergleich zum Plastik-Szintillationsdetektor werden unterschiedliche Amplituden der Asymmetrie erwartet. Um die Auswirkungen der Asymmetrie auf den Bias in der Position des Schauerkerns zu bestimmen, werden Studien zur Entwicklung der Asymmetrie für beide Detektoren durchgeführt.

Unter der Verwendung simulierter Luftschauer, die durch ein Proton ausgelöst werden und EPOS-LHC als hadronisches Modell verwenden, wird eine Parametrisierung abgeleitet, welche den Bias in der Position des Schauerkerns sowohl für Wasser-Cherenkov-Detektoren als auch für Plastik-Szintillationsdetektor korrigiert. Zu diesem Zweck werden zahlreiche Regressionsanalysen durchgeführt, um die Abhängigkeiten der Amplitude der Asymmetrie von Entfernung, Zenit Winkel und Energie zu beschreiben. Das abgeleitete Modell für den Wasser-Cherenkov-Detektor wird auf die Daten angewendet und die Verbesserungen anhand des Bias und der Auflösung der Kernposition bewertet. Die Anwendung des abgeleiteten Modelles auf die Daten, korrigiert den Bias in der Position des Schauerkerns zu einem verbleibenden Bias unter  $\pm 10$  m und verbessert die Kernauflösung um  $\sim 20$  bis zu 40 m.



# Contents

<b>1. Introduction</b>	<b>3</b>
<b>2. Generalities about Cosmic Rays</b>	<b>5</b>
2.1. Cosmic Rays . . . . .	5
2.1.1. Discovery . . . . .	5
2.1.2. Energy Spectrum . . . . .	6
2.1.3. Candidate Sources . . . . .	7
2.1.4. Detection . . . . .	8
2.2. Extensive Air Showers . . . . .	8
2.2.1. Definitions . . . . .	9
2.2.2. Shower Characteristics . . . . .	11
<b>3. The Pierre Auger Observatory</b>	<b>13</b>
3.1. Fluorescence Detector . . . . .	13
3.2. Surface Detector . . . . .	14
3.3. AugerPrime Upgrade . . . . .	15
3.4. Reconstruction of the Lateral Profile . . . . .	17
<b>4. Analysis of the Asymmetry in Signals</b>	<b>19</b>
4.1. Introduction of the Bias . . . . .	19
4.1.1. Geometrical Effect . . . . .	19
4.1.2. Longitudinal Attenuation . . . . .	20
4.1.3. Asymmetry in Simulated Events . . . . .	20
4.2. Analysis Approach and Statistical Methods . . . . .	22
4.2.1. Fitting Procedure . . . . .	22
4.2.2. Analysis Settings . . . . .	22
4.2.3. Analysis Structure . . . . .	23
4.3. Results of the Amplitude of the Asymmetry . . . . .	25
4.3.1. Electromagnetic Component . . . . .	25
4.3.2. Muonic Component . . . . .	27
4.3.3. Total Amplitude . . . . .	27
4.4. Correction of the Asymmetry . . . . .	31
4.4.1. Dependency on Distance . . . . .	31
4.4.2. Dependency on Zenith Angle . . . . .	37
4.4.3. Dependency on Energy . . . . .	44
4.5. Derived Model . . . . .	45
4.5.1. Impact on the Core Position . . . . .	45
4.5.2. Impact of the Asymmetry on the Shower Size . . . . .	47
4.5.3. Comparison with Existing Model . . . . .	47
<b>5. Conclusion and Outlook</b>	<b>49</b>

<b>Appendix</b>	<b>51</b>
A. Fit Parameters Dependency on Distance . . . . .	51
B. Fit Parameters Dependency on Zenith Angle . . . . .	53
<b>Bibliography</b>	<b>59</b>

# Acronyms

<b>CR</b>	Cosmic Ray
<b>EAS</b>	Extensive Air Shower
<b>LDF</b>	Lateral Distribution Function
<b>FD</b>	Fluorescence Detector
<b>WCD</b>	Water-Cherenkov Detector
<b>SSD</b>	Scintillator Surface Detector
<b>UHECR</b>	Ultra-High-Energy Cosmic Ray
<b>LHC</b>	Large Hadron Collider
<b>SNR</b>	SuperNova Remnant
<b>KASCADE</b>	KARlsruhe Shower Core and Array DETector
<b>CMB</b>	Cosmic Microwave Background
<b>GRB</b>	Gamma-Ray Burst
<b>AGN</b>	Active Galactic Nuclei
<b>PMT</b>	PhotoMultiplier Tube
<b>HEAT</b>	High Elevation Auger Telescopes
<b>UV</b>	UltraViolet
<b>VEM</b>	Vertical-Equivalent Muon
<b>HG</b>	High-Gain
<b>LG</b>	Low-Gain
<b>MIP</b>	Minimum Ionizing Particle
<b>SD</b>	Surface Detector
<b>WLS</b>	WaveLength-Shifting
<b>NKG</b>	Nishimura-Kamata-Greisen
<b>AMIGA</b>	Auger Muon and Infill for the Ground Array
<b>ADF</b>	Angular Distribution Function



# 1. Introduction

Since the discovery of Cosmic Rays (CRs) more than 100 years ago, scientists have been working to complete the knowledge of high-energy particles arriving from outer space. CRs have been observed with energies up to  $10^{20}$  eV. Such high energies are not accessible in man-made particle accelerators. The flux of CRs at these energies, with only one particle per  $\text{km}^2$  per year, is so low, that large ground-based detector arrays are needed. Indeed, once the particles reach the Earth, they interact with molecules of the atmosphere, initiating a cascade of particles also known as Extensive Air Shower (EAS). These EAS consist of a large number of secondary particles passing through the Earth's atmosphere to finally reach the ground. The largest ground-based detector ever built is the Pierre Auger Observatory, located in the Argentinean Pampa. The Pierre Auger Observatory is using two independent detection methods. The first technique consists of 27 fluorescence telescopes, which are installed at four different sites to observe the longitudinal development of the air showers. This allows the determination of a reliable estimator of the mass composition of the incoming primary particles. In addition, a grid of 1660 Water-Cherenkov Detectors (WCDs) is spread over  $3000 \text{ km}^2$ , to measure the particle density on ground [2]. The particle density is modeled as a function of the distance from the shower axis, with the Lateral Distribution Function (LDF) enabling the reconstruction of shower parameters of the primary particle. Those shower parameters are the impact point of the shower axis, the shower size or the arrival direction.

The particle density of the measured signals on ground was believed to be rotationally symmetric around the shower axis. In reality, the lateral distribution of signals is asymmetric, due to a combination of geometrical and attenuation effects. The discrepancy of the used rotationally symmetric model and the asymmetric reality leads to a systematic error in the reconstructed observables. To correct the azimuthal asymmetry in the measured signals of WCDs, a model has been developed in [1]. Currently, the Pierre Auger Observatory is upgraded by the installation of a Scintillator Surface Detector (SSD) on top of each WCD. This instrumental upgrade intends to improve the determination of mass composition at high energies. However, due to the different detector responses for the components of an EAS, different amplitudes of asymmetry are expected for SSDs and WCDs.

This thesis aims at a deeper understanding of the evolution of the asymmetry in SSDs. Therefore, the asymmetry of different shower components for SSDs and WCDs is studied. In addition, a parametrization for the detectors is developed to correct the azimuthal asymmetry in signals. The correction of the model is expected to decrease the bias in the reconstructed shower parameters. In particular, exact knowledge of the position of the shower core is of great interest, since it is required to estimate the energy of the CR.

Chapter 2 introduces the general properties of CRs and the necessary theoretical basics are explained. Chapter 3 provides insight into the structure of the Pierre Auger Observatory. In Chapter 4, the simulated data is analyzed to develop a model that corrects the bias in the position of the shower core caused by the azimuthal asymmetry in signals.



## 2. Generalities about Cosmic Rays

Since Cosmic Rays (CRs) were discovered in 1912 by Victor Hess during balloon flights, many experiments were conducted and many discoveries were found [3]. In search for answers to the fundamental questions of the evolution and structure of the universe, scientists have worked in cloud chambers, climbed high mountains or taken balloon flights to investigate the nature and origins of CRs. Nowadays, particle detectors are mounted on satellites launched in space, or deployed over a large ground-based array observing Extensive Air Showers (EASs). Although we have learned a lot about CRs, our knowledge is not yet complete. This chapter provides an overview of this knowledge and the theoretical background on which this thesis is based.

### 2.1. Cosmic Rays

CRs are high-energy charged particles traveling through large distances at almost the speed of light before reaching the Earth. Figure 2.1-left illustrates the energy spectrum of CRs, whose understanding plays an essential role in the study of cosmic particles. The minimum energy a CR must have to penetrate the magnetized solar wind and reach the Earth is  $10^9$  eV [4]. The highest energy particles are called Ultra-High-Energy Cosmic Rays (UHECRs) and have been observed, so far, with an energy up to  $10^{20}$  eV [5]. In comparison, the world's most powerful particle accelerator, Large Hadron Collider (LHC), can only reach energies of up to  $10^{17}$  eV [6]. Thus, these particles from outside our solar system have the highest energies ever observed and are far from reproducible with our current technology. The flux of CRs is continuous in energy and is following, as a function of the energy, a power-law proportional to  $\propto E^{-\gamma}$ , with the spectral index  $\gamma \approx 3$ . Before entering into the different features of the spectrum, in Section 2.1.2, the discovery of CRs is discussed in more details.

#### 2.1.1. Discovery

In 1909, the physicist Theodor Wulf built a new electrometer, which had an enhanced sensitivity and transportability than the common electroscopes of that time [7]. T. Wulf performed several measurements at different places, with the will to test the common theory that the measured ionizing radiation originates from the natural radioactivity, discovered a decade ago. Therefore, a decrease of the radiation rate with increasing altitude is expected. One of his measurement sites was the Eiffel Tower, nearly 300 m above the ground. But the decrease in the radiation rate at that height was far less than expected [8].

Two years later, Victor Hess pursued the research. He achieved measurements at greater heights using hot air balloons. During the first flights, altitudes up to 1100 m were reached [9]. In these measurements, the electrometer recorded a lower radiation rate than on the ground. During a flight in the year 1912, a maximum height of 5300 m was reached. Above 2000 m an increase in the radiation rate was found, which was about three times higher than the value on the ground [9]. Based on this discovery, V. Hess assumed that these radiations, unlike previously suspected, do not originate from the Earth's crust, but enters our planet

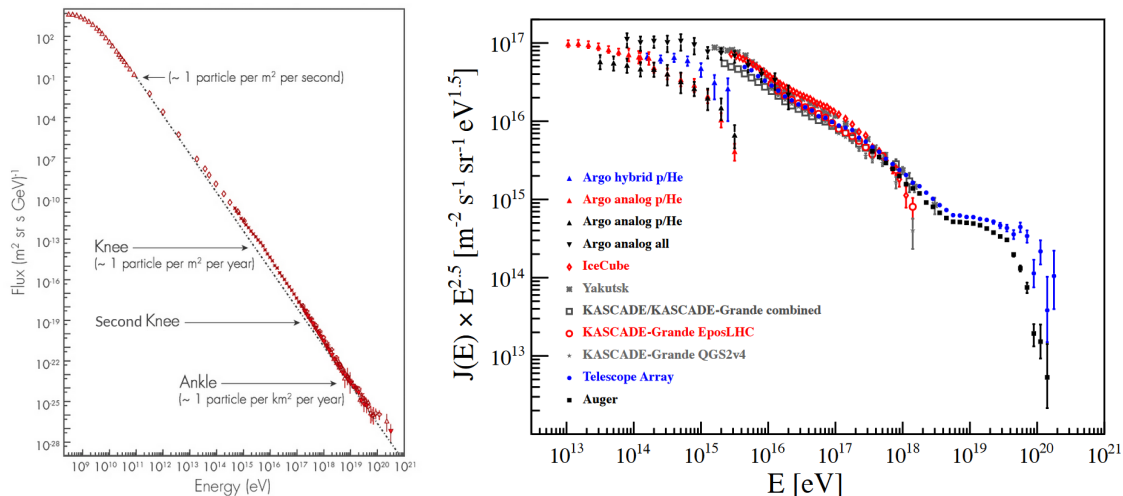


**Figure 2.1.:** *Left:* Energy spectrum of CRs. Figure extracted from [11]. *Right:* Energy spectrum of UHECRs. The spectrum is multiplied by  $E^{2.5}$ , to make the characteristic features more visible. Figure extracted from [12].

from outer space. Moreover, V. Hess did not measure a significant decrease in the radiation rate at a flight during a partial solar eclipse, avoiding the Sun to be the source of these radiations [10]. V. Hess discovered cosmic radiation and thus laid the foundations of a new era of exploration of our Universe, which is still ongoing.

### 2.1.2. Energy Spectrum

The spectrum in energy, meaning the flux of CRs as a function of the energy, is presented in Figure 2.1. About 10 000 particles with energies of 10<sup>9</sup> eV reach the Earth per square meter every second. This rate decreases very quickly with increasing energy. Only a few particles with energies about 10<sup>16</sup> eV arrive per square meter per year, while only one particle above 10<sup>19</sup> eV reaches the Earth per square kilometer per year [11].

The total spectrum is composed of the sum of the spectra of different constituents with different spectral indices  $\gamma$  in different energy regimes. A well-describing simplified approximation of the spectrum is a single power-law proportional to  $\propto E^{-\gamma}$  with a spectral index of around  $\sim 3$ . Nevertheless, there are a few spectral features that break that regularity. The origin of these characteristic features is still a topic of current studies, even though numerous promising theories have been put forward. Figure 2.1-left, depicts the flux of CRs covering the full range of energy. Up to an energy of 10<sup>14</sup> eV, the flux is large enough that the particles are measured directly with detectors located on balloons or satellites [13]. At these low energies, the flux consists mainly of protons and other light nuclei. Because of the low flux at energies above 10<sup>14</sup> eV, the flux can only be measured by experiments observing air showers. Figure 2.1-right, shows a zoom of the energy spectrum, emphasizing the spectral features breaking the regularity of the spectrum. The flux is rescaled by a factor of  $E^{2.5}$ , as the characteristics of the spectrum appears more clearly in that range. Around  $3 \times 10^{15}$  eV, the first spectral feature is observed in form of a slight kink in the spectrum [12]. This steepening of the flux is denoted as *knee*. It is commonly assumed that the origin of the knee is associated with the end of acceleration of CRs by Galactic sources, such as SuperNova Remnants (SNRs) [14]. Assuming that the maximum acceleration energy of a given particle is proportional to its mass, the light elements like protons are the first particles reaching their maximum acceleration energy. Gradually, heavier particles, up to iron, reach their maximum potential of acceleration, resulting in the *second knee* at an energy of around  $\sim 10^{17}$  eV [12]. One can remark that this second steepening of the spectrum is less marked than the first one. To investigate this theory, among others, the

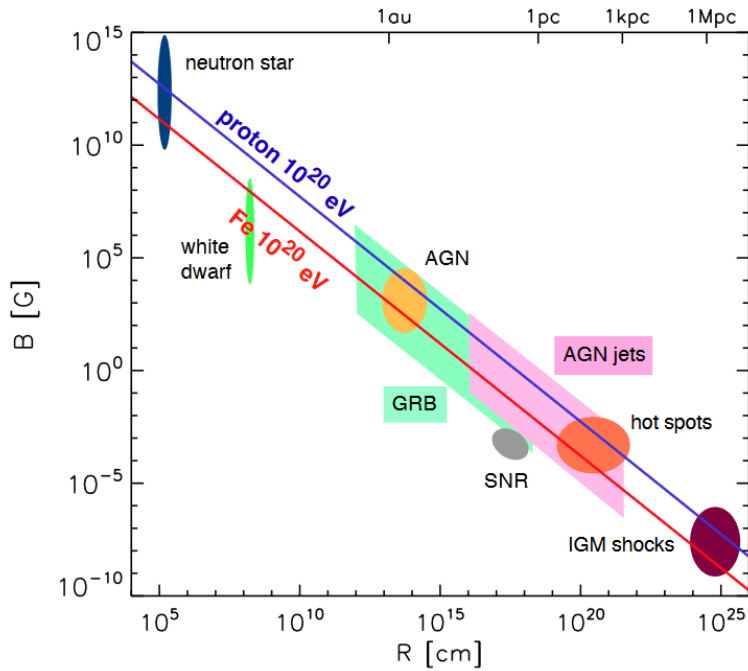


**Figure 2.2.:** Hillas diagram of candidate sources. The local magnetic flux density  $B$  is plotted as a function of the radius of the acceleration region  $R$ . On top of the common candidate sources, the maximum energy reachable for proton (blue line) and iron (red line) are reported. Figure extracted from [20].

KARlsruhe Shower Core and Array DETector (KASCADE) has examined this energy range extensively. They observed a change from heavy to light elements, which is consistent with the previous hypotheses [15]. Thus, the origin of the first knee could be attributed to a decrease of the light component of the flux, while the second knee is explained by a decrease of heavier components.

After reaching the second knee, the highest possible energy of the SNR for iron has been achieved, which leads to a decrease of the flux. However, at  $\sim 5 \times 10^{18}$  eV, an increase of the spectrum is observed, denoted as the *ankle* [12]. This increase could be explained by a change of sources. Thanks to studies about the arrival directions of CRs, it is generally assumed that the ankle is a result of the transition from Galactic to extragalactic sources. At  $\sim 6 \times 10^{19}$  eV, a strong suppression of the flux is observed [12]. The origin of this sharp steepening is still under investigation. An attempt of explanation arises from the assumption that the accelerators outside our Galaxy have reached their upper limit for the maximum acceleration energy. A second, and complementary explanation lies in propagation effects, such as the influence of magnetic fields and the interaction with backgrounds such as the Cosmic Microwave Background (CMB). The latter one leads to energy loss due to pion production and is also known as the GZK-effect, named after the work of Greisen [16], Zatsepin and Kuzmin [17].

The composition of CRs, depends strongly on their energy. For example low-energy CRs, below  $10^{13}$  eV, are composed of light nuclei, especially protons. Above  $10^{18}$  eV, the fraction of heavier nuclei increases with energy [18]. The composition of the CRs is summarized as follows: About 89% of the arriving particles are protons, another 10% are helium nuclei and the remaining 1% are heavier nuclei [19].

### 2.1.3. Candidate Sources

In parallel of the study of the spectrum, studies about the candidate sources of UHECRs are conducted. An impeding effect for tracing UHECRs back to their source is deflection.

After a charged particle escapes from its source, it is interacting with the particles and magnetic fields it encounters. As a result, the arrival direction observed from Earth does not necessarily coincide with the direction of its origin. However, CRs with higher energies are significantly less deflected by magnetic fields. The direction of arrival could therefore be associated with the direction of known celestial objects with more confidence. Thus, selecting light elements constitutes the next challenge in the study of UHECRs.

Each candidate source of UHECRs has an energy limit to which particles are confined. Assuming that the Larmor radius should not exceed the radius of the acceleration region, the maximum energy has the form:

$$E_{\max} \sim q \cdot B \cdot R, \quad (2.1)$$

where  $q$  denotes the electric charge of the particle,  $B$  describes the strength of the magnetic field and  $R$  designate the radius of the acceleration region. Figure 2.2 shows a Hillas diagram and depicts candidate sources for UHECRs, which are collected using their known characteristics. For a given maximum energy  $E_{\max}$ , the Hillas plot visualizes the relation between the strength of the magnetic field  $B$  of a candidate source and its size. Above the diagonal lines a source is able to accelerate a proton or an iron nuclei to a maximum energy up to  $10^{20}$  eV.

The knee, shown in Figure 2.1, is suspected to be the end of acceleration of protons by SNRs. Particles which have energies below the ankle are assumed to have a Galactic origin, while particles with energies above the ankle are assumed to have an extragalactic origin [21]. Possible Galactic sources could be type II supernovae, the shock fronts of SNRs or pulsars. As shown in Figure 2.2, potential extragalactic sources include Gamma-Ray Bursts (GRBs), neutron stars and Active Galactic Nuclei (AGN) [22]. However, a source for UHECRs with energies above  $10^{20}$  eV has not yet been discovered.

Although the exact sources are not yet known, advancements are expected with a better understanding of the mass, energy and arrival direction of the CRs.

#### 2.1.4. Detection

CRs can either be measured directly or indirectly. Direct measurement can only take place above the Earth's atmosphere. Therefore, the detectors must be located on satellites, space stations or very high-altitude balloons. Detecting an event with energies above  $10^{19}$  eV is difficult, because the flux of CRs at such high energies is tiny. Only one extremely high energetic particle per square kilometer reaches the Earth's atmosphere on average per year. The detectors in space are not large enough to observe a significant number of these events. The ground-based detectors are used to overcome this issue and thus, measure these high energy particles indirectly, by observing the secondary particles produced after the interaction of a CR with molecules of the atmosphere. On ground, an observation of the secondary particles is possible by building a large surface of detection, or by measuring the UltraViolet (UV) radiation, emitted by the deexcitation of the molecules of the atmosphere. Indirect measurements on Earth are exemplary performed by the Pierre Auger Observatory, which is discussed, in more details, in Chapter 3. The design of the Pierre Auger Observatory has been imagined to use all the methods developed to observe UHECRs indirectly.

## 2.2. Extensive Air Showers

When a CR enters the upper atmosphere, it collides with air molecules. This collision creates secondary particles. A so-called EAS is initiated. Secondary particles from the collision interact with other air molecules and create a cascade of particles. Thus, knowing the properties of this cascade, the properties of the primary particle are inferred.

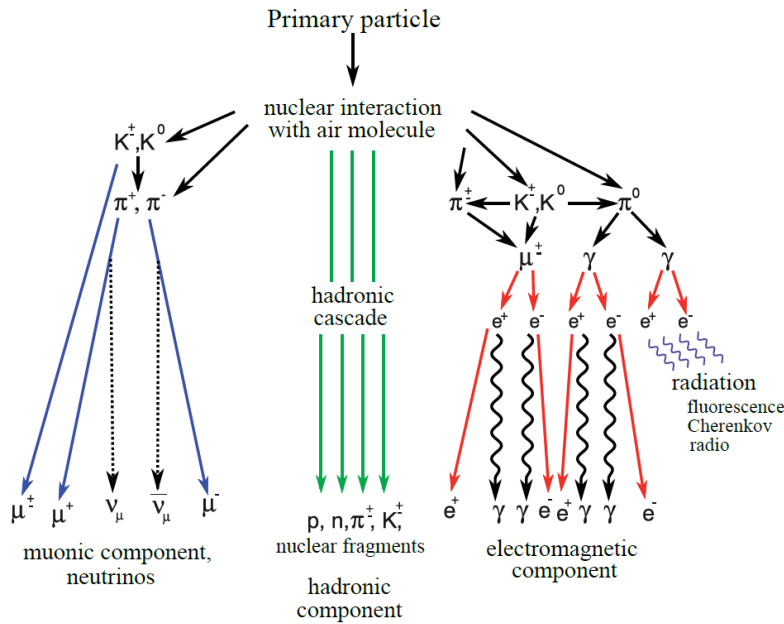


**Figure 2.3.:** Schematic view of the development of an EAS, which is induced by a cosmic primary particle. The air shower is divided into the electromagnetic, the hadronic and the muonic component. Figure extracted from [23].

### 2.2.1. Definitions

In 1934, Bruno Rossi made a pioneering measurement. He was able to discover EAS by setting up multiple detectors at a specific distance and measuring simultaneous events in neighboring detectors. In 1938, Pierre Auger and his students performed measurements at the Jungfraujoch in the Swiss Alps. They also discovered the arrival of particles at spatially spread detectors almost simultaneously [24]. Thanks to the number of particles in an air shower, P. Auger et al., estimated the energy of the primary particle to be about  $10^{15}$  eV. The work about EAS was also driven by Schmeiser, Bothe and Kolhörster [25]. They conducted further experiments with air showers. In the process, the first interconnected detector arrays were developed.

An EAS is composed of three components, the electromagnetic component, the hadronic component and the muonic component. The development of an exemplary air shower is illustrated in Figure 2.3. In the first stages of the shower development, the *hadronic component* plays an essential role. After the nuclear interaction of a primary CR with air molecules in the upper atmosphere, hadrons, especially pions, are produced as the first particles of the EAS. The hadronic component consists of nuclear fragments, protons, neutrons, pions and kaons [26]. Due to the instability of pions and kaons, they either interact with further air molecules, creating new pions, or decaying into other particles. As soon as the pion energy drops below a critical level, most particles decay and no longer interact with other particles. The decay process of neutral pions, formulated as

$$\pi^0 \rightarrow \gamma + \gamma, \quad (2.2)$$

results in an electromagnetic subshower [27].

The *electromagnetic component* consists of photons, electrons and positrons. Heitler and Matthews introduced a simple model of electromagnetic cascades, which can also be applied to the hadronic shower component [27]. The model states, that each particle travels a collision length  $\lambda$  through the atmosphere, before undergoing a branching process at a certain depth  $X$  [26]. The two-body splitting takes place either through pair-production or bremsstrahlung processes. The energy of the particle is distributed equally between the two

particles being created. After  $n = X/\lambda$  numbers of splitting, the total amount of particles in the shower is  $N = 2^n$ . At a certain threshold  $E_c$ , the individual energy of the particles is too low for further pair-production or bremsstrahlung processes. In air, the threshold of this critical energy is  $E_c = 85 \cdot 10^6$  eV [27]. Below this energy level, no new particles are generated and the increase of particles comes to an abrupt end. According to the model of Heitler and Matthews, the final total number of particles  $N(X_{\max})$  is proportional to the energy  $E_0$  of the primary CR. The maximum number  $N(X_{\max})$  of particles in an air shower is reached, when all particles have the energy  $E_c$ . This leads to an energy

$$E_0 = E_c \cdot N(X_{\max}), \quad (2.3)$$

of the primary particle. Thus, the shower maximum is expressed as:

$$X_{\max} = \lambda \cdot \frac{\ln(E_0/E_c)}{\ln 2}. \quad (2.4)$$

Due to the long distances inclined shower particles have to travel in the atmosphere, the electromagnetic component is largely absorbed before reaching the ground. The absorption occurs after  $X_{\max}$  is reached, in particular by low-energy ionization processes and the photoelectric effect [28].

Finally, muons and neutrinos belong to the *muonic component*. They are mainly caused by the decay of charged pions and kaons. The common decay of charged pions is the decay into a muon and a muon neutrino:

$$\pi^+ \rightarrow \mu^+ + \nu_\mu, \quad (2.5)$$

$$\pi^- \rightarrow \mu^- + \bar{\nu}_\mu. \quad (2.6)$$

The dominant decay mode of charged kaons is the leptonic decay into a muon and a muon neutrino:

$$K^+ \rightarrow \mu^+ + \nu_\mu, \quad (2.7)$$

$$K^- \rightarrow \mu^- + \bar{\nu}_\mu. \quad (2.8)$$

The semileptonic decay occurs less frequently and is expressed as

$$K^+ \rightarrow \pi^0 + \ell^+ + \nu_\ell, \quad (2.9)$$

$$K^- \rightarrow \pi^0 + \ell^- + \bar{\nu}_\ell, \quad (2.10)$$

with  $\ell = e, \mu$ . Within the weak hadronic decay, the kaons decay to pions:

$$K^+ \rightarrow \pi^+ \pi^0, \quad (2.11)$$

$$K^- \rightarrow \pi^- \pi^0, \quad (2.12)$$

$$K^+ \rightarrow \pi^+ \pi^+ \pi^-, \quad (2.13)$$

$$K^- \rightarrow \pi^- \pi^- \pi^+. \quad (2.14)$$

Because of the lower interaction rate of muons with matter, most of them traverse the atmosphere without being attenuated [19]. Apart from deflections due to the geomagnetic field and energy losses based on ionization, non-decaying muons survive to the ground [28]. Thanks to that, muons are a reliable tracker for the mass of the primary CR, that has initiated the EAS.

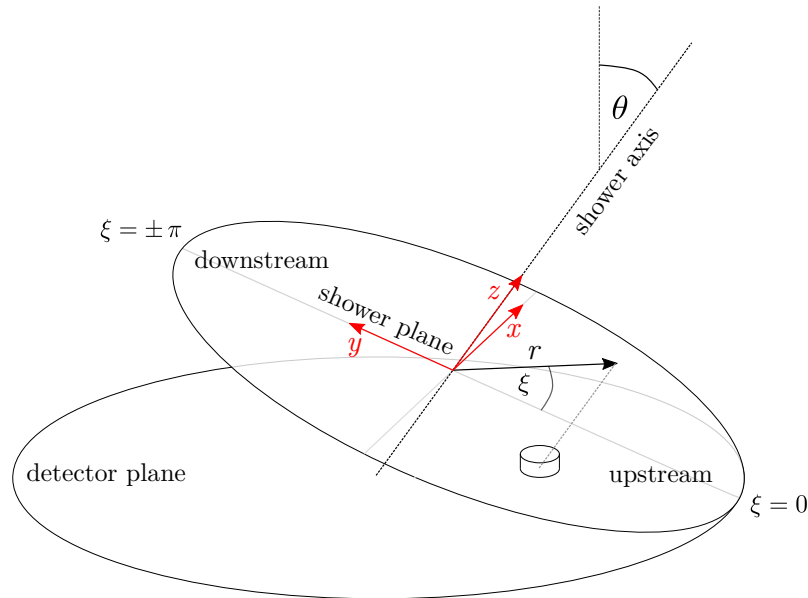


**Figure 2.4.:** Schematic view of the shower coordinate system. During the reconstruction process, either the shower plane or the ground plane are used to describe the characteristics of the shower. The intersection of the shower axis with the shower plane is denoted as the shower core and coincides with the coordinate origin. Figure adapted from [1].

### 2.2.2. Shower Characteristics

Figure 2.4 illustrates a schematic view of the geometry of an incoming air shower. The arrival direction of a shower is marked by the shower axis and is defined by the zenith angle  $\theta$  and the azimuth angle  $\varphi$ . The azimuth is defined according to the East direction of the Pierre Auger Observatory. The inclination of a shower is determined by the zenith angle  $\theta$ , which is defined as the angle between the shower axis and the local zenith. The plane perpendicular to the shower axis is referred to the shower plane. The intersection of the shower axis with the shower plane is denoted as the shower core. The corresponding coordinate system is defined such that the origin of the coordinate system coincides with the shower core in the shower plane. The  $z$ -axis is pointing towards the shower axis and the  $x$ - $y$ -plane corresponds to the shower plane.

The area on the ground, where the detector array is located, is called the detector or ground plane. Each detector has a distance  $r$  from the shower axis in the shower plane. Depending on where the detectors are positioned, they have different polar angles  $\xi$  in the shower plane. The polar angle describes the angle between the projection of the arrival direction to the shower plane and the vector connecting the shower core and the position of the detector. Using this definition, the shower plane is divided into two different regions. The area for  $|\xi| < \pi/2$  is denoted as *upstream* (or *early*) region, while for the *downstream* (or *late*) region,  $|\xi| > \pi/2$  applies. The polar angle  $\xi$  is also referred as azimuth angle of a detector in the shower plane.

The profile along the shower depth is denoted as longitudinal profile and describes the evolution of the number of particles during the development of the shower. Gaisser and Hillas established a function that describes the longitudinal shower development [29]. One can imagine the lateral shower profile as the "footprint" of an air shower on the ground. The lateral distribution describes the density of particles as a function of the distance from the shower axis. The lateral profile is presented in more detail in Chapter 3.



## 3. The Pierre Auger Observatory

Due to the tiny flux of CRs at the highest energies, the Pierre Auger Observatory uses ground-based indirect detection methods. The Pierre Auger Observatory is located in Mendoza, the western part of Argentina and was built to detect EAS initiated by UHECRs. In addition to the Fluorescence Detector (FD) observing the longitudinal development of an air shower by collecting the emitted UV light, the lateral distribution of the secondary particles of an EAS is measured by the Surface Detector (SD) on the ground. The SD of the Pierre Auger Observatory is spread over an area of  $3000 \text{ km}^2$ , which is approximately 17 times the size of Karlsruhe. Since the particles of a cascade are distributed over an area of  $16 \text{ km}^2$ , it is possible to collect a large number of events even at the highest energies [2]. Figure 3.1 shows the full area of the Pierre Auger Observatory. The black dots illustrate the position of the 1660 detector tanks of the SD, while the four star-shaped lines represent the locations of the 27 fluorescence telescopes. The two methods of observing UHECRs indirectly are independent of each other, defining the Pierre Auger Observatory as a “hybrid detector”.

### 3.1. Fluorescence Detector

The FD consists of 27 fluorescence telescopes in four different places. Each of the four sites contains six fluorescence telescopes, which overlook the SD array. Figure 3.2-left shows one of the sites with the telescopes behind the opened shutters. The three remaining fluorescence telescopes are part of the High Elevation Auger Telescopes (HEAT). They

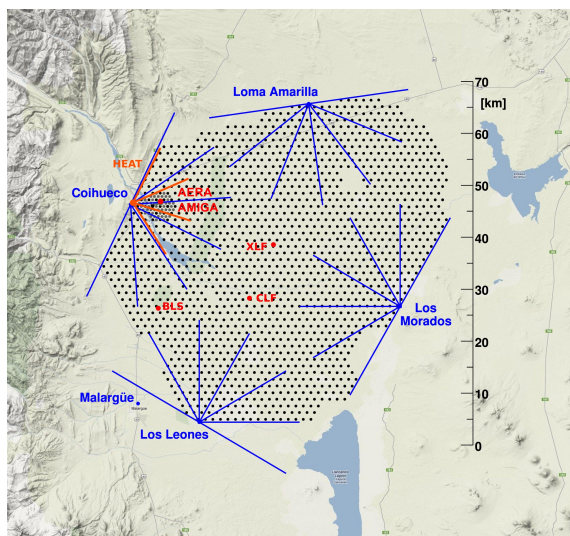


**Figure 3.1.:** Map of the SD array of the Pierre Auger Observatory. Each black dot represents the location of a SD station. The fields of view of the fluorescence telescopes are illustrated with radial blue lines. Figure extracted from [30].



**Figure 3.2.:** Setup of the FD of the Auger Observatory. *Left:* Picture of one of the four sites, which contains six fluorescence telescopes, each telescope overlooking part of the SD with an azimuth and elevation of  $30^\circ$ . Figure extracted from [2]. *Right:* Schematic setup of a single fluorescence telescope. The UV light of an EAS is collected and focused on a camera by a grid of segmented mirrors. Figure extracted from [31].

are located in separated inclined containers and are able to observe the atmosphere at greater heights. The FD can only collect data on a cloudless and moonless night. Thus, the duty-cycle is only assured at 15% of the operating time [32]. When a CR enters the Earth's atmosphere, it interacts with the air molecules, provoking, among other effects, the emission of UV light in response. These photons are collected by one of the telescopes of the FD. That way, the FD is measuring the longitudinal development or longitudinal profile of the EAS. Figure 3.2-right shows schematically the setup of a single fluorescence telescope. Each telescope is located behind a window with a circular aperture system and a UV filter. In case the telescope is not in operation, the shutter is closed to protect the sensitive instruments. The incident UV light is collected by a large segmented spherical mirror and get focused on pixels, the PhotoMultiplier Tubes (PMTs) [2]. The PMTs convert the light into an electrical signal with a magnitude dependent on the intensity of the measured light.

### 3.2. Surface Detector

A single SD station is composed of a water tank and the associated readout electronics, power supply and communication system. The SD of the Pierre Auger Observatory consists of a triangular grid of 1600 Water-Cherenkov Detector (WCD) stations <sup>1</sup>, where each detector station is 1.5 km away from its neighboring stations [2]. The higher the energy of a primary particle, the larger is the “footprint” of an EAS on the ground. The large distances between the stations are designed for the detection of UHECRs. When an EAS hits the ground, a large amount of secondary particles zipping through several SD tanks. Comparing the signals from the different SD tanks enables the reconstruction of various shower parameters of the primary particle, such as the energy.

Figure 3.3-left shows the setup of a single WCD station. Each WCD tank is filled with 12 000 liters of highly purified water. When a charged particle of an EAS enters the WCD station, the particle passes through the water. If these particles are moving faster than the speed of light in water, Cherenkov radiations are emitted. When a charged particle travels through a dielectric medium, the medium becomes electrically polarized. As soon as the particles are passing, the molecules of the medium fall back to their ground state through emission of light. This light radiates spherically from its point of emission and grows at the speed of light, while the particle moves faster than the sphere grows. The particle now emits light in the medium at many different locations. Each time the light leaves the emission point in a growing sphere. The edges of the many spheres overlap and

<sup>1</sup>In addition, there are about 60 stations within the Auger Muon and Infill for the Ground Array (AMIGA), that are half the distance of the regular array.

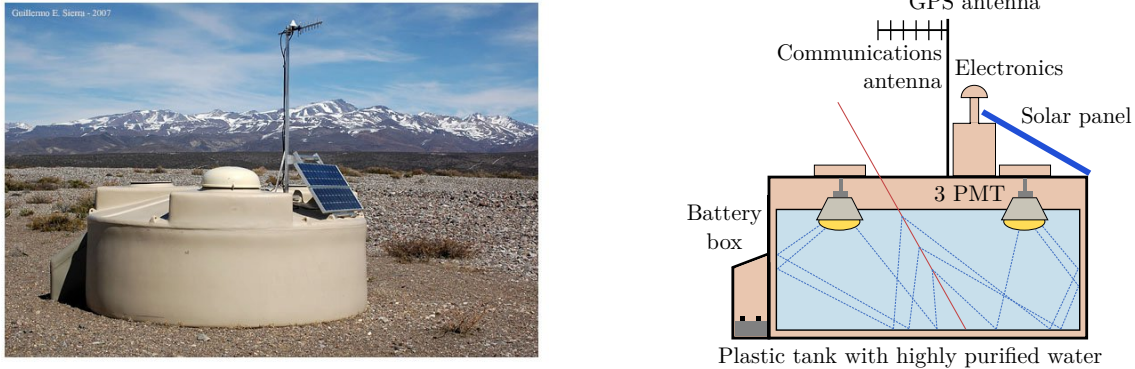


**Figure 3.3.:** Setup of the SD of the Pierre Auger Observatory. *Left:* Picture of a single WCD tank located in the Argentinean Pampa. Figure extracted from [36]. *Right:* Schematic setup of a WCD with its main components. The particles are measured because of their interaction with water in the SD tanks. Figure adapted from [31].

form a wave front. As a result, the Cherenkov light is emitted conical around the path of the charged particle and is observed as a blue glow [33].

The travel of the emitted Cherenkov photons in a SD tank is depicted in Figure 3.3-right. The path of an incident particle through water is illustrated with the red line. The blue lines outline the photons from the Cherenkov emission, measured by the three PMTs, which are installed on top of the SD tank. The recorded signals are measured in units of the signal generated by a vertically and centrally passing muon with an energy of 1 GeV. This is known as a Vertical-Equivalent Muon (VEM) [34]. The PMTs transform the energy of the Cherenkov photons into electrical signals. These signals are sent and processed on the electronics, which are installed on top of the tank. The signals are taken from the last dynode and from the anode of each PMT. The signals from the last dynode are amplified and therefore denoted as the High-Gain (HG) signals while the signals of the anode are called Low-Gain (LG) signals. In case of high energy CRs, a high flux is entering the station and could cause the saturation of the HG signals. In this situation, the integration is performed with the LG signals. For even larger flux, the LG signals may also go into saturation. In that case, a recovery procedure is performed in which a signal-recovery algorithm attempts to restore the missing traces of the PMTs [35].

The data is transferred via a communication antenna to the receiving station. With the help of a GPS antenna it is possible to measure the exact timing of the signal's entry. Charged by photovoltaic panel, 2 batteries of 12V are providing the energy to the whole acquisition system.

### 3.3. AugerPrime Upgrade

Currently, the SD of the Pierre Auger Observatory is undergoing an upgrade process, called “AugerPrime”. Part of the upgrade consists on adding a 4 m<sup>2</sup> Scintillator Surface Detector (SSD) on top of each WCD station. This will provide an accurate distinction between the muonic and electromagnetic component of an air shower. Furthermore, the installation of new SD station electronics and the addition of a small PMT on the WCD, for a widened dynamic range, is under deployment too. Moreover, the new electronics should improve timing accuracy and increase the sampling rate. The observatory will also receive a radio upgrade and the limited duty cycle of the FD is to be improved, which is intended to increase the amount of hybrid data at high energies [32].

A picture of an already upgraded SD station is illustrated in Figure 3.4-left. On top of the WCD, the SSD is to be installed. The radio antenna is part of the AugerPrime radio upgrade. Since SSDs are not effective for large zenith angles, the radio upgrade adds an array-based composition sensitivity to measure larger zenith angles [39].

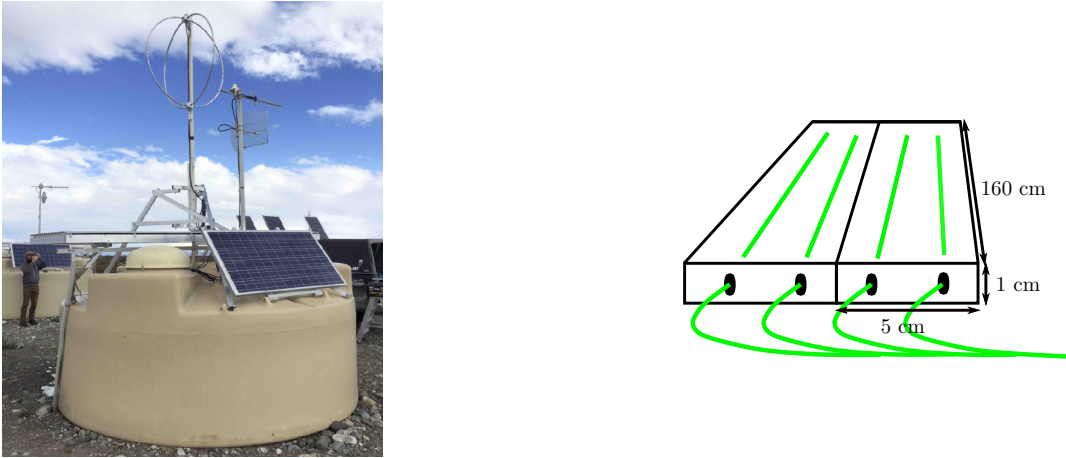


**Figure 3.4.:** Setup of the SD of the Pierre Auger Observatory after the AugerPrime upgrade. *Left:* Picture of an already upgraded SD station. An SSD is installed on top of the WCD tank. Figure extracted from [37]. *Right:* Schematic setup of two scintillator bars containing the fiber readout. Figure adapted from [38].

The main idea behind the upgrade is to enable a more precise determination of the mass composition of high energy particles, which may help to trace the sources. Collecting more data in this energy range, could additionally help to find the origin of the flux suppression at the highest energies. The improvement of the sensitivity to mass composition will also improve the study about hadronic interaction, that support the development of EAS [38]. Especially for WCDs and SSDs, the different detector responses to the components of an EAS are a big advantage. SSDs are more sensitive to the electromagnetic component of the shower, while for WCDs the combination of the muonic and electromagnetic component is more complex.

The electromagnetic shower component has a lower penetration depth into the water of the WCD. The muonic component has a larger energy deposit in water. These two different detector responses provide a complementary measurement and enable a more precise determination of the muonic and electromagnetic shower components at ground level.

Only the main feature of the upgrade, which contains the placement of the SSD on top of each WCD, is relevant to the work presented in this thesis. For this reason, the SSD will be discussed in more details below. The SSD is based on two modules. Each module is a plane built of 24 extruded polystyrene scintillator bars. One scintillator bar is 160 cm long, 5 cm wide and 1 cm high. The active area of the scintillator amounts to  $3.8 \text{ m}^2$  [40]. Each bar has two holes in it, which insert the readout mechanism of WaveLength-Shifting (WLS) fibers. When a charged particle enters the scintillator, its material absorbs part of the energy of the particle, which leads to a re-emission of the absorbed energy through light. The scintillator light is collected by the fibers, which are connected to a single PMT. The PMT absorbs the emitted photons and utilizes the photoelectric effect to convert the photons into an electrical signal.

Figure 3.4-right shows the concept of two bars containing the fiber readout. On the external side of each module, the fibers are arranged in a semicircle. This arrangement should maximize the light yield [38].

The signal for SSDs is measured in units of Minimum Ionizing Particle (MIP), which embody charged particles with a minimum mean energy loss rate in substances.

The bars and fibers are embedded in an aluminum frame. The bottom of this frame is built of extruded polystyrene. Expanded polystyrene is filling the spaces left between the bars and fibers [40].

Reading the data for the SSD runs in *slave mode*. This means, when the corresponding

WCD reports a trigger, the SSD data is read out too, no matter if a particle is passing through the SSD or not, which could lead to zero SSD traces. This trigger algorithm, which only applies to the WCD, has the disadvantage that small signals, that would trigger the SSD but are insufficient to trigger the WCD, are not recorded and get lost.

### 3.4. Reconstruction of the Lateral Profile

The Pierre Auger Collaboration has developed a framework in which scientists can work together on algorithms to develop all the necessary applications. The so-called *Offline software framework* supplies the required infrastructure for the analysis of the measured data. To be an usable software framework for the collaboration of many physicists, it has to have certain properties. Since application development is a lengthy process, the code must be stable and flexible enough to implement different applications from time to time. Furthermore, the code must allow the simulation and reconstruction of the events in the different detector types and must be able to handle greatly variable data. The Offline software framework must be expandable in the way that further upgrades to the detectors, such as the current AugerPrime upgrade, can be implemented in the code. In addition, each collaborator should be able to implement the algorithm he or she develops in the software. The software is written in C++, an object-oriented programming language.

In general, the Offline framework is segmented in three different parts. The simulation and reconstruction algorithms are structured in *modules*. These modules can readout the data from the *detector description* and the *event data*. The detector description includes the characteristics of the various detectors and time-dependent atmospheric conditions. The event data contains all data about simulation and reconstruction methods. After data processing, the new reconstructed information is added to the event data.

An important reconstruction task of the Offline framework is the reconstruction of the lateral profile to derive the properties of the primary particle. The SD of the Pierre Auger Observatory measures the lateral distribution of an EAS on the ground. The density of particles as a function of the distance  $r$  from the shower axis in the detector plane is modeled with the Lateral Distribution Function (LDF). Unfortunately, the shape of the true LDF and the true shower sizes of most events are unknown due to the sparsely triggered stations and all the uncertainties about the signals. To overlook that problem, a scaled average LDF  $f_{\text{LDF}}(r)$ , derived from the data, is used to fit the signals from the stations, which is expressed as follows

$$S(r) = S(r_{\text{opt}})f_{\text{LDF}}(r). \quad (3.1)$$

Here  $f_{\text{LDF}}$  is normalized, such that  $f_{\text{LDF}}(r_{\text{opt}}) \equiv 1$  is valid.  $S(r_{\text{opt}})$  is denoted as the estimator of the shower size, which is equal to the number of particles in a shower at a particular level and distance. The shower size is related to the energy of the primary CR. For this reason,  $S(r_{\text{opt}})$  is also an estimator of the energy of the primary particle, even though the reconstruction is more difficult because of fluctuations in the shower development [35].

An optimal value for the distance  $r_{\text{opt}}$  has been determined to minimize the fluctuations due to the lack of knowledge of the true LDF. The optimal distance  $r_{\text{opt}}$  is dependent on the structure of the detector array. The optimal value for the Pierre Auger Observatory is  $r_{\text{opt}} \approx 1000$  m. For this reason, in this thesis,  $S(1000)$  will be referred as the estimated parameter of the shower size. The approach of the LDF utilizes a modified Nishimura-Kamata-Greisen (NKG) function. This LDF model is referred to the *Observer* reconstruction and is expressed as

$$f_{\text{LDF}}(r/\text{m}) = \left(\frac{r}{r_{\text{opt}}}\right)^{\beta} \left(\frac{r+r_{\text{s}}}{r_{\text{opt}}+r_{\text{s}}}\right)^{\beta+\gamma}, \quad (3.2)$$

with  $r_s = 700$  m [35]. The slopes  $\beta$  and  $\gamma$  are dependent on the shower size  $S(1000)$  and the zenith angle  $\theta$ . To fit the LDF for the signals in WCDs, signals for at least three stations of the SD array are needed because three parameters are fitted: the shower size  $S(1000)_{\text{WCD}}$  and the coordinates  $(x, y)$  of the intersection of the shower axis with the detector plane. For SSDs, only one station is needed since the position of the core is already fixed by the WCD reconstruction. Since a SSD is mounted on top each WCD station, the position of the shower core at the ground, used for fitting WCD signals, can also be used for fitting SSD signals. Hence, only one station with an SSD signal is necessary to fit the LDF.

At the end of the reconstruction process, files with the simulated data are created. To process the large amounts of data, the software framework ROOT is used [41]. The simulated data is provided in ADST files, where the data is represented in a columnar data set, denoted as the *TTree*. Each independent column is also called a *branch*, which is referenced to multiple *leaves*. The tree structure can thus be seen as a collection of interconnected nodes. This tree data structure enables a hierarchical way of storing and processing data. The structural coherence of the data becomes clear and allows a flexible handling of the data.

A simulated event is characterized by different parameters, such as the event ID, the azimuth angle, the core position or the energy of the primary particle. Since the lateral profile of an event is sampled by several detector stations, a sublist of station parameters is available for each station that has triggered. The information, varying from detector to detector, is saved in each detector description. Such information may include detector geometry, atmospheric conditions, or constants required for calibration [42].

## 4. Analysis of the Asymmetry in Signals

This chapter describes the analysis of the azimuthal asymmetry in signals measured with both, WCDs and SSDs. The analysis is performed using a simulated data set of air showers initiated by a proton primary using EPOS-LHC as hadronic model [43]. Performing the study with simulations is necessary since the true energy, mass, and position of the core of the shower needs to be known. The set of simulations has a continuous library in zenith angle from  $0^\circ$  to  $65^\circ$  and is continuous in energy from  $E_{\min} = 10^{18.5}$  eV to  $E_{\max} = 10^{20}$  eV. Since the full efficiency of the detector is achieved only up to  $60^\circ$ , angles above  $60^\circ$  are not considered.

The first part of Chapter 4 explains the problem with azimuthal asymmetry and why it needs to be solved. The required statistical methods are introduced and the analysis approach is described. The differences between WCDs and SSDs in the amplitudes of the asymmetry for the different shower components are elucidated and a model correcting the asymmetry for both, SSDs and WCDs is derived. For the moment, the reconstruction of the core position is performed using WCD data only, thus, only the model for WCDs is tested in this thesis. For this purpose, the improvements of the applied model are given in terms of the core bias and resolution.

### 4.1. Introduction of the Bias

For a rotationally symmetric shower, initiated by CRs with a zero zenith angle, the cross section of an EAS with the detector plane is expected to be a concentric circle around the shower axis. For inclined showers, the footprint of the EAS on the ground is expected to have an elliptical symmetry around the shower axis. Only projecting the measurements from the detector plane to the shower plane would recover the circular symmetry [44].

In reality, however, the lateral distribution of the EAS on the ground is more complex than assumed. Thus, in addition to the geometrical effect previously mentioned, effects occurring during the travel of particles from their emission to the ground, have to be taken into account. In the following two sections, the two main effects that cause the asymmetry in signals are discussed in more detail.

#### 4.1.1. Geometrical Effect

The particles of an EAS spread in a cone in the atmosphere. When the particles reach the ground, they are measured by several detectors, which have different distances  $r$  to the shower axis and different polar angles  $\xi$ . Due to their various locations in the detector plane and the inclination of the shower, they have different zenith angles  $\theta_p$  (compare Figure 4.1). The zenith angles of the incoming particles are larger on a station at the downstream side in contrast to the upstream side. Figure 4.1 shows two detectors within the detector plane. The late plane, the core plane and the early plane illustrate shower fronts that intersect the detector plane at different stages in shower development. First, particles of the early plane reach the ground. At last, particles of the late plane enter the Earth's surface. These particles have larger zenith angles and have traveled a longer

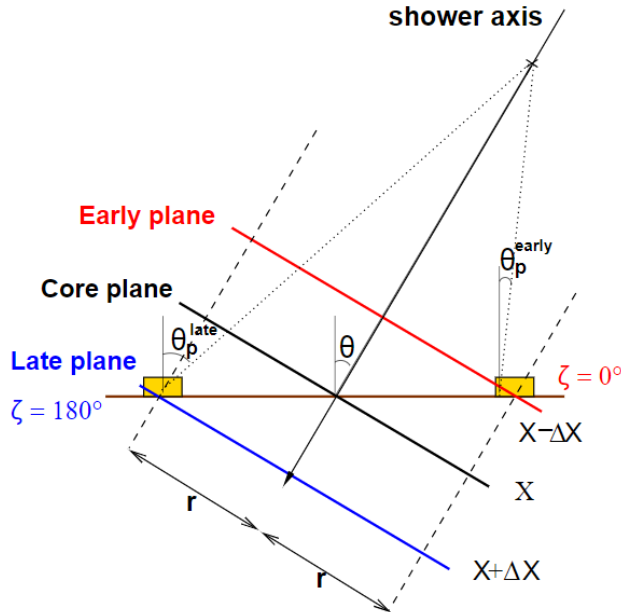


**Figure 4.1.:** Schematic depiction of an incident shower with non-zero zenith angle  $\theta_p$ . The three planes intersect the detector plane at different depths of shower development. Figure extracted from [28].

distance through the atmosphere, than particles in the early region.

The effective area  $A_{\text{eff}}$  of the detector is composed of the top area  $A_{\text{top}}$  and the side wall areas  $A_{\text{side}}$  of the tanks and is expressed as

$$A_{\text{eff}} = A_{\text{top}} \cdot \cos(\theta_p \pm \alpha) + A_{\text{side}} \cdot \sin(\theta_p \pm \alpha). \quad (4.1)$$

The positive sign refers to the downstream stations, while the negative sign refers to the upstream stations. The angle  $\alpha$  is defined as the angle of emission [45].

The impact of the geometric effect is assumed to depend on the type of detector. For example the detector responses to electromagnetic particles are expected to be affected by this dependency in zenith angle, resulting in a geometrical asymmetry. The amplitude of the asymmetry for muons is expected to be around zero, since for the light deposit by muons in water only the volume of the tank is of importance. Non-inclined showers are expected to be symmetric. Showers with a large zenith angle are assumed to be dominated by muons, which implies low values for the asymmetry. Therefore, the more inclined the shower, the lower is the expected amplitude of the signal [45].

#### 4.1.2. Longitudinal Attenuation

At the same distance  $r$  from the shower axis, the density of particles in the upstream region is higher than in the downstream region. Particles that reach the ground on the upstream side travel a shorter path through the atmosphere. They therefore depict an earlier stage of shower development. After the shower reaches its maximum during its longitudinal development, the intensity of the shower begins to decrease due to attenuation in the atmosphere. As a consequence of its longer travel distance, especially the electromagnetic component gets more attenuated when reaching the downstream side.

#### 4.1.3. Asymmetry in Simulated Events

In inclined showers, an azimuthal asymmetry of the signals is observed, caused by a combination of geometrical and attenuation effects. Figure 4.2 illustrates a 2D distribution of the

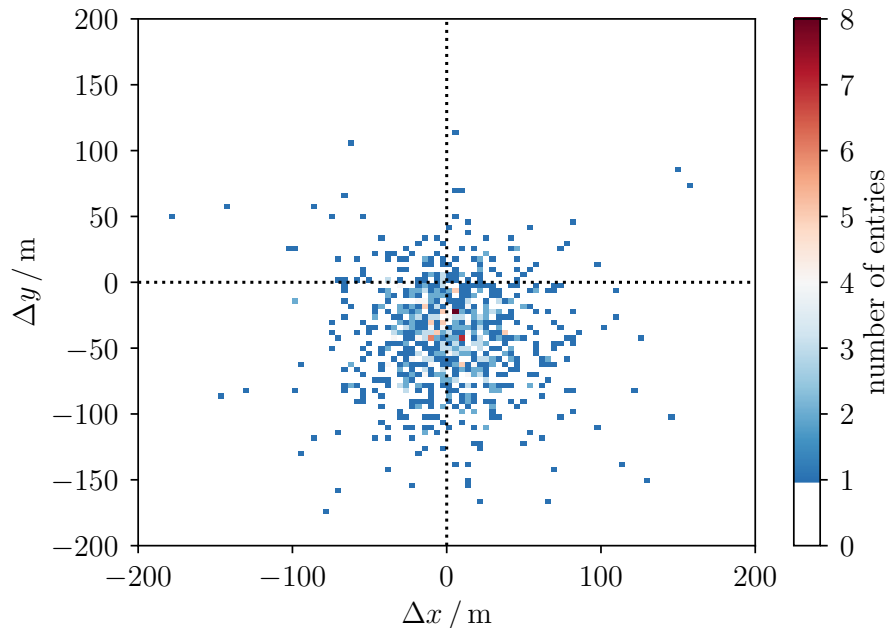


**Figure 4.2.:** Scatter plot of  $\Delta x = x_{\text{rec}} - x_{\text{MC}}$  against  $\Delta y = y_{\text{rec}} - y_{\text{MC}}$ . The index “MC” relates to the simulated values and the index “rec” to the reconstructed values. The color scale of the 2D distribution shows the number of entries.

reconstructed core position into the simulated shower plane. Each data point illustrates the occurrence of a simulated event with a certain zenith angle  $\theta_{\text{MC}}$  and an impact point  $(x_{\text{MC}}, y_{\text{MC}})$ , within the shower plane coordinate system, at which the shower axis hits the ground. The parameters, reconstructed using the Offline framework described in Section 3.4, are denoted  $\theta_{\text{rec}}$  for the reconstructed zenith angle and  $(x_{\text{rec}}, y_{\text{rec}})$  for the reconstruction position of the impact point. In the shower plane coordinate system, the  $y$ -component describes the upstream-downstream direction, while the  $x$ -component defines its perpendicular direction. The shower plane coordinate system is presented in Section 2.2.2. The  $\Delta x$  and  $\Delta y$  components describe the differences between the simulated and reconstructed coordinates of the shower core.

The 2D distribution in Figure 4.2 shows, that the distribution is not centered around the origin of coordinates, but is shifted into the upstream direction, due to geometrical and attenuation effects. This observed azimuthal asymmetry in the shower plane, influences the reconstruction of the observables, such as the position of the shower core, and introduces a bias. The shower core is shifted on average by about  $\sim 40$  m in the upstream direction. For showers with an inclination of  $\sim 45^\circ$ , the bias increases to  $\sim 70$  m up to  $\sim 80$  m. To reduce this bias in the reconstructed observables, it is necessary to study the evolution of the azimuthal asymmetry as a function of the inclination of the shower, the distance from the shower axis and the energy of the primary particle initiating the air shower. After the impact on the reconstructed observables has been determined, a parametrization is derived, which corrects the resulting bias. Especially the position of the shower core is of importance, as it is used to determine an estimate for the energy of the CR. A model to correct this azimuthal asymmetry in signals measured by the WCD has already been created [1]. However, as part of the AugerPrime upgrade, a SSD is currently being installed on top of each WCD. Since WCDs and SSDs have different detector responses to the muonic and electromagnetic component of an EAS, the model needs to be further developed. For that purpose, the investigation of how azimuthal asymmetry behaves in signals measured by the SSDs and how it affects the reconstructed observables is necessary. In addition, it is examined whether the current model is affected by the installation of

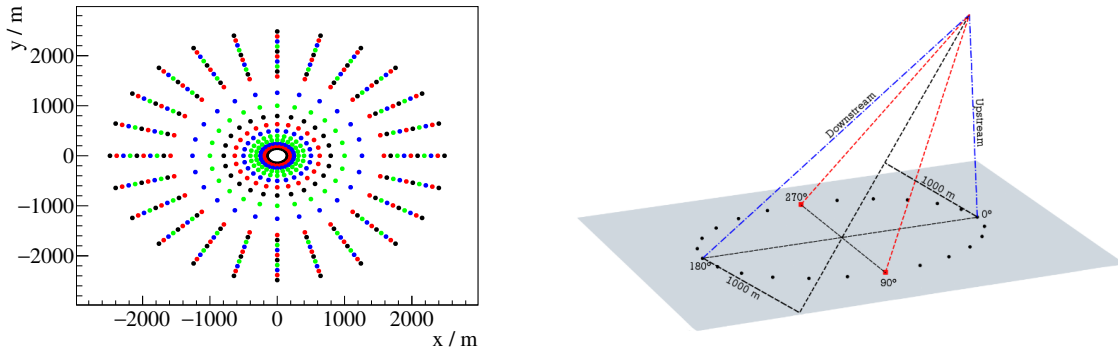


**Figure 4.3.:** *Left:* Map of the distribution of dense rings within the detector plane. Each dense ring consists of 24 detector stations. *Right:* Dense ring at  $r = 1000$  m from the shower axis. Figure extracted from [47].

SSDs on top of WCDs or not. Once the new model has been developed, it is compared to the already existing parametrization of the azimuthal asymmetry.

## 4.2. Analysis Approach and Statistical Methods

In this section, the analysis developed in this thesis to study and correct the azimuthal asymmetry in signals is explained by introducing the analysis settings and statistical methods. The statistical analysis in this thesis is performed using regression analysis.

### 4.2.1. Fitting Procedure

Regression analysis is a statistical analysis method used to describe the relation between dependent and independent variables. The parameters of a fit function are recovered in such a way that they describe the data best. The regression analysis utilized in this thesis is performed using the MINUIT framework [46]. For the adjustment of the parameters, the builtin cost function of a general weighted least-squares fit `iminuit.cost.LeastSquares` is used. The least squares method is briefly explained below.

Assuming a plain data set  $(X_i, Y_i)$  with  $i = 1, \dots, n$ . The variable  $X_i$  denotes the independent variable, while  $Y_i$  represents the dependent variable. The least-squares method calculates the difference between the real data  $Y_i$  and the value provided by the model function  $f(X, \sigma)$ . This difference is denoted as a residual

$$R_i = Y_i - f(X_i, \sigma). \quad (4.2)$$

The sum of the squared residuals

$$S_R = \sum_{i=1}^n R_i^2, \quad (4.3)$$

is minimized to obtain the best parameters for the model function. To use a least-square fit, the  $y$ -error must be specified. If the  $y$ -error is specified incorrectly, the resulting fits could be biased.

### 4.2.2. Analysis Settings

As described in Section 3.4, the information of simulated events is stored in ADST files. Such files contain the energy of the primary particle, the core position, the zenith angle and a list of stations with station ID, distance  $r$ , polar angle  $\xi$  and the measured total unsaturated signal  $S(r, \xi)$ . As introduced in Section 3.2, a high flux could cause the saturation of the signals. In this thesis, the total unsaturated signal  $S(r, \xi)$ , meaning the integrated signal of trace without the saturation processes, is used. Therefore, the

**Table 4.1.:** Distances  $r$  from the shower axis for the different dense rings.

distances $r$ / m			
0	1	2	3
158.5	199.5	251.2	316.2
794.3	630.9	501.2	398.1
1684.9	1584.9	1258.9	1000.0
2084.9	1984.9	1884.9	1784.9
2484.9	2384.9	2284.9	2184.9

performed study is possible even close to the shower core.

A distinction is made between stations of the dense rings (station ID  $> 90000$ ) and stations of the main array (station ID  $< 5000$ ). For the analysis, only stations that belong to one of the 20 dense rings are considered. Figure 4.3-left depicts a map of the distribution of the simulated dense rings, located within the detector plane. Each dense ring consists of 24 detector stations and has a fixed distance  $r$  from the shower axis. Due to limited computational capacity of 2 GB memory, each simulated event is recreated four times with rings at different distances from the shower axis. The distances are given in meters and are listed in Table 4.1. At first, the distances follow a natural logarithmic function and above 1500 m they are chosen to have a distance of 100 m from its neighboring dense rings. Figure 4.3-right, illustrates an inclined shower measured by the stations of the dense ring at a distance of  $r = 1000$  m from the shower axis.

The measured signals depend on the energy and zenith angle of the CR and on the distance from the shower axis. Since the set of simulations have a continuous library in energy and zenith angle, it is useful to bin these variables. In the search for the most suitable number of bins, various numbers were investigated by using histograms. There should be just enough bins to smooth out fluctuations without losing information. For the zenith angle, a binning of eight bins in  $\sin^2 \theta$  is set. Using a binning in  $\sin^2 \theta$ , instead of a binning in  $\theta$ , results in a flat distribution with almost the same number of events per bin. For the energy, a linear binning with 15 bins in  $\lg(E/\text{eV})$  is chosen. The measured signals are considered separately in each dense ring.

### 4.2.3. Analysis Structure

The basic approach of the analysis is shown as a block diagram in Figure 4.4. The presented procedure is applied to the data from both detectors, SSDs and WCDs. In a first step, the total amplitude of the asymmetry is depicted. For this purpose, the total unsaturated signal  $S(r, \xi)$ , divided by its expected signal  $\langle S(r, \xi) \rangle$ , according to Eq. 3.1, is plotted as a function of the polar angle  $\xi$ . Since the true LDF is not known, an estimator for  $\langle S(r, \xi) \rangle$  is obtained by calculating the mean of the 24 stations belonging to a dense ring. The total unsaturated signal

$$S_{\text{total}} = S_{\text{EM}} + S_{\mu}, \quad (4.4)$$

results from the sum of the electromagnetic unsaturated signal component  $S_{\text{EM}}$  and the muonic unsaturated signal component  $S_{\mu}$ . Since WCDs and SSDs respond differently to the signals from the electromagnetic and muonic shower component, it is useful to observe these two components separately. To obtain the muonic signal, the sum of several subtraces must be formed. This results in

$$S_{\mu} = S_{\text{MuonTrace}} + S_{\text{PhotonFromMuonTrace}} + S_{\text{ElectronFromMuonTrace}} + S_{\text{HadronicTrace}}, \quad (4.5)$$

with the traces built from the interaction of muons ( $S_{\text{MuonTrace}}$ ) and hadrons ( $S_{\text{HadronicTrace}}$ ) in the tank. The traces from photons or electrons that have decayed from muons (respectively  $S_{\text{PhotonFromMuonTrace}}$  and  $S_{\text{ElectronFromMuonTrace}}$ ) are also considered.

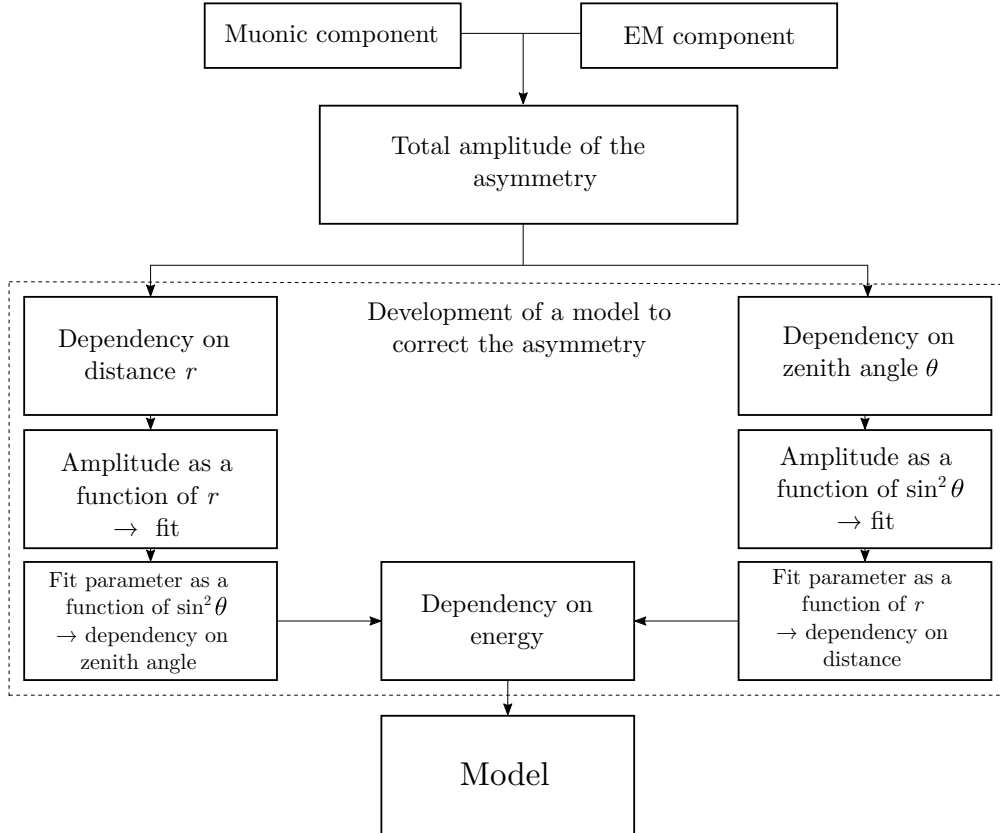


**Figure 4.4.:** Structure of the Analysis, presented in a block diagram. The total amplitude of the asymmetry is decomposed into its components to better compare SSDs and WCDs. Subsequently, a model for the correction of the asymmetry is developed that takes the dependence on the distance  $r$ , the zenith angle  $\theta$  and the energy  $E$  into account.

The electromagnetic component results from the sum of signals from photons ( $S_{\text{PhotonTrace}}$ ) and electrons ( $S_{\text{ElectronTrace}}$ ):

$$S_{\text{EM}} = S_{\text{PhotonTrace}} + S_{\text{ElectronTrace}} \cdot \quad (4.6)$$

The extracted signals of the shower components are plotted as a function of the polar angle  $\xi$ . By fitting the signals for WCDs and SSDs, the amplitude of the asymmetry  $\alpha(r, \theta)$  is extracted. The fit function is expressed as

$$S(r, \xi) = \langle S(r, \xi) \rangle [1 + \alpha(r, \theta) \cos \xi], \quad (4.7)$$

with  $\langle S(r, \xi) \rangle$  and  $\alpha(r, \theta)$  as the two fitting parameters.

The extracted amplitudes of the asymmetry for the electromagnetic and the muonic components are plotted as a function of the distance  $r$ . A comparison of the amplitudes for WCDs and SSDs will provide important insights into the different detector responses as a function of the distance. The signals for SSDs are mainly the results of interactions with electromagnetic particles. Thus, the amplitude of the asymmetry is largely driven by the electromagnetic shower component. For WCDs, the combination of the muonic and electromagnetic component is more complex.

To derive a model to correct the asymmetry in signals, a clear view of the evolution of the amplitude of the asymmetry with distance and zenith angle needs to be developed, to test the hypotheses formulated in Section 4.1.1 and 4.1.2. To achieve this, the total amplitude  $\alpha(r, \theta)$  of the asymmetry is plotted as a function of the distance  $r$ . Based on

that distribution, a model function needs to be formulated, that describes the data best. Subsequently, the resulting fit parameters are plotted as a function of  $\sin^2 \theta$ . The fitting process is repeated and another model function must be found that describes the data.

A different approach to develop the same model considers the dependency in zenith angle  $\theta$  first. The total amplitude  $\alpha(r, \theta)$  of the asymmetry is plotted as a function of  $\sin^2 \theta$ . After a suitable model function has been found, the resulting fit parameters are presented as a function of the distance  $r$ . The fit procedure is performed again, resulting in a model function which describes the data best. As a last step, the two models are tested at different energies to ensure that the observed results are consistent for all energies.

### 4.3. Results of the Amplitude of the Asymmetry

Figure 4.5 shows the distribution  $f(\xi) = S(r, \xi) / \langle S(r, \xi) \rangle$  as a function of the polar angle  $\xi$ . To obtain a better comparison of the asymmetry at different distances, the total unsaturated signal  $S(r, \xi)$  is divided by its expected signal. The expected signal is calculated using Eq. 3.1. Since the true LDF is not known, the mean signal  $\langle S(r, \xi) \rangle$  of the 24 stations belonging to a dense ring is used as a more precise estimator than using the LDF with an unknown true shape.

The results for  $19.4 < \lg(E/\text{eV}) < 19.5$  and  $0.3 < \sin^2 \theta < 0.4$  at the four different distances  $r = 158.5 \text{ m}$ ,  $501.2 \text{ m}$ ,  $1000 \text{ m}$  and  $1584.9 \text{ m}$  from the shower axis, are illustrated in Figure 4.5. The distances are chosen, because the signals at the optimal distance  $r_{\text{opt}} = 1000 \text{ m}$  are used to determine the shower size, as described in Section 3.4. For this reason, it is promising to observe the signals at distances closer and further away than  $r_{\text{opt}}$ .

Signals measured with SSDs are shown on the left side of the figure, while signals measured with WCDs are shown on the right side of the figure. By fitting the distributions for WCDs and SSDs, the amplitude of the asymmetry  $\alpha(r, \theta)$  is extracted. For the fitting procedure, the non-normalized signals  $S(r, \xi)$  are plotted as a function of the polar angle  $\xi$ . Then, the distributions are fitted with Eq. 4.7. Plotting  $S(r, \xi) = f(\xi)$ , instead of  $S(r, \xi) / \langle S(r, \xi) \rangle = f(\xi)$ , helps to prevent an underestimation of the fitted amplitude. A particle on the downstream region travels a longer path through the atmosphere and is therefore more attenuated. Subsequently, it is possible that some of the dense stations in the downstream side are not triggering. Some dense rings might be incomplete and thus biasing the mean value of the signal to higher values. Using  $S(r, \xi) = f(\xi)$  avoids the influence of the previously calculated distorted mean signal  $\langle S(r, \xi) \rangle$ . By fitting  $\langle S(r, \xi) \rangle$ , all events in a bin are taken into account, which leads to an equal normalization for all events. However, to better compare the graphs visually, the plots of the normalized signals are presented in this thesis.

The plots of the total amplitude of the azimuthal asymmetry in Figure 4.5 for WCDs and SSDs, are revealing interesting differences between the responses of the two detectors. The blue dots illustrate the mean value of the different events with the standard deviation as error bars. Close to the shower axis, the amplitude of the asymmetry for SSDs and WCDs looks very similar, but this similarity decreases with growing distance from the shower axis. As a function of the distance, the amplitude of the asymmetry increases for both, WCDs and SSDs. Approximately above  $r = 1000 \text{ m}$ , the amplitude of asymmetry for SSDs is greater, compared to WCDs. To find the origin of these differences between the detectors, it is useful to split the total signal into its components.

#### 4.3.1. Electromagnetic Component

To investigate the behavior of the electromagnetic component in more detail, Figure 4.6 depicts the amplitude  $\alpha_{\text{EM}}$  for the electromagnetic component as a function of the distance  $r$ . The amplitude of the asymmetry for SSDs is shown on the left, while the amplitude of the asymmetry for WCDs is shown on the right. The colors represent different values for bins

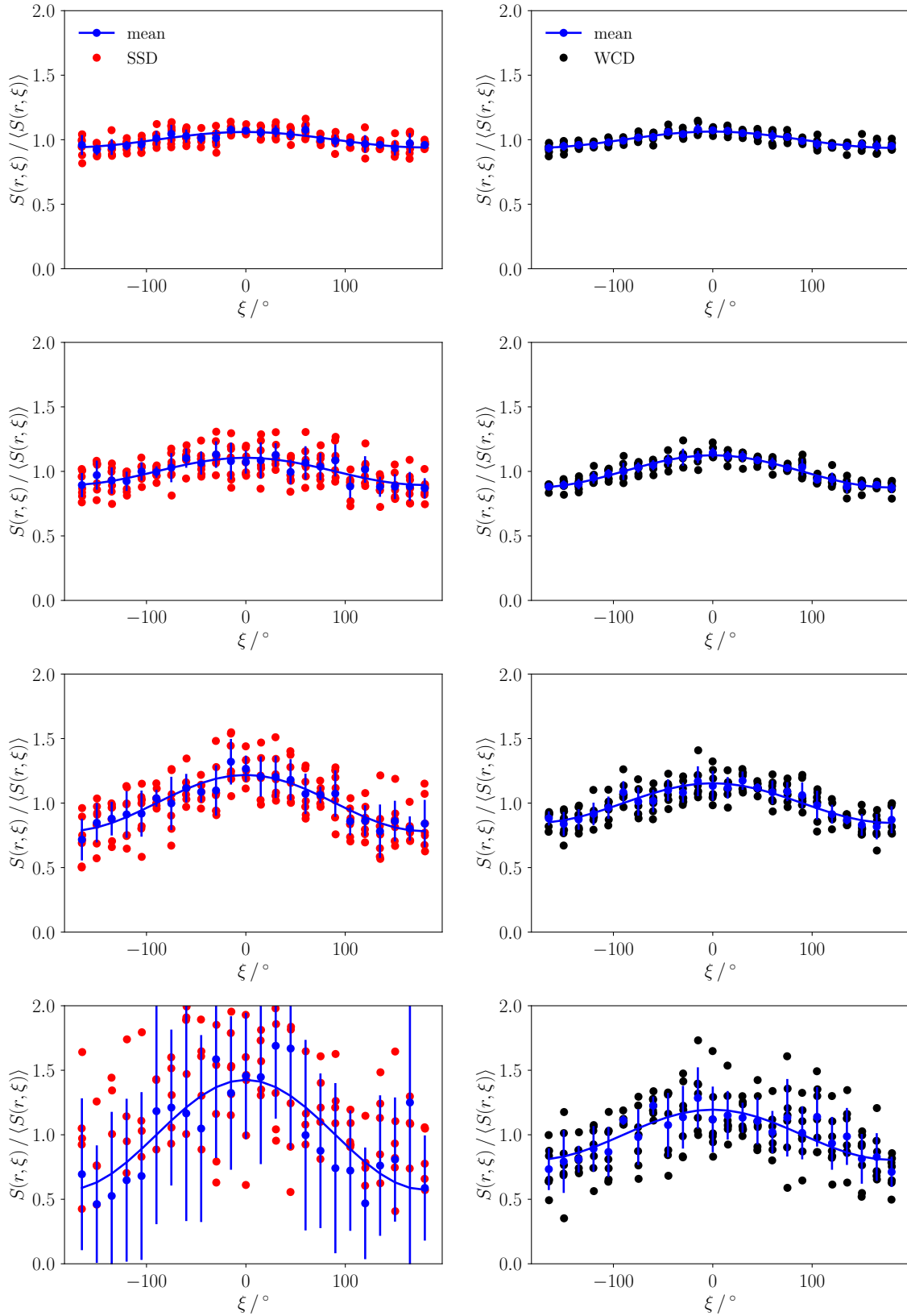


**Figure 4.5.:** The total amplitude of the asymmetry at four different distances from the shower axis. From top to bottom, the distances are  $r = 158$  m, 501 m, 1000 m and 1584 m. The distributions use simulated showers which are generated by a proton primary with energies between  $19.4 < \lg(E/\text{eV}) < 19.5$  and with zenith angles between  $0.3 < \sin^2 \theta < 0.4$ . *Left:* Signals measured with SSDs. *Right:* Signals measured with WCDs.

in  $\sin^2 \theta$  in radian: 0.05 (dark blue), 0.15 (orange), 0.25 (dark green), 0.35 (red), 0.45 (light green), 0.55 (grey), 0.65 (purple) and 0.75 (light blue). For both detectors, the asymmetry of the electromagnetic component increases with distance. The function first rises steeply and then becomes flatter. With increasing distance from the shower axis, the asymmetry of the electromagnetic component, caused by the geometrical and attenuation effect, increases. This is consistent with the hypothesis formulated in Section 4.1.1 and 4.1.2. For showers with a small zenith angle ( $\sin^2 \theta \approx 0.05$ ), the amplitude of the asymmetry is close to zero. The higher the inclination of the shower axis, the higher is the amplitude of the asymmetry. However, for large zenith angles ( $\sin^2 \theta \approx 0.75$ ), large uncertainties are observed and the signals get noisy, especially for SSDs. At large distances and/or large zenith angles, the electromagnetic component is increasingly absorbed, because of the greater distances the particles travel through the atmosphere. This leads to noise in the measured signals. With higher energy of the primary CR, the distance to which the signals are measured in a detector station increases. By comparing the plots for SSDs and WCDs at the same energy of the CR, it is noticeable that WCDs have more statistically significant data than SSDs at large distances.

### 4.3.2. Muonic Component

The amplitude of the asymmetry  $\alpha_\mu$  as a function of the distance for the muonic shower component is illustrated in Figure 4.7. The amplitude of the asymmetry for SSDs is shown on the left, while the amplitude for WCDs is shown on the right. For WCDs, at close distances, the amplitude  $\alpha_\mu$  for the muonic component is around zero, as expected. Thus, the geometrical effect dominates the distribution for small distances. At large distances, however, it seems that the amplitude of asymmetry for muons is decreasing into negative values. At large distances, both asymmetry causing effects, mentioned in Section 4.1.1 and 4.1.2, need to be considered. As derived in [48], the amplitude of the asymmetry is proportional to

$$\alpha \propto 2 - \gamma + \frac{d(\theta)}{\lambda}, \quad (4.8)$$

with the distance  $d(\theta)$  between the point of emission of the particle (assuming a conical model) and the position of the detector and  $\lambda$ , the attenuation length (different for each type of particles considered). The parameter  $\gamma$  corresponds to the exponent of the Angular Distribution Function (ADF) and the factor 2 originates from the solid angle under which the shower is seen by the detector. If  $\gamma > 2 + \frac{d(\theta)}{\lambda}$  applies, a negative amplitude of the asymmetry occurs. The angle under which the particles are emitted varies, depending on whether the particle is measured by a detector on the downstream or upstream side. The angle of emission on the downstream side is smaller than the angle on the upstream side. The larger the distance from the shower axis, the larger is the angle of emission and the smaller is the number of particles arriving at ground. However, due to the small cross-sections of muons, their attenuation is less dominant and at large distances there are more muons in the downstream side than in the upstream side. Thus, the muonic component has a negative amplitude of the asymmetry for long distances. The decrease begins at an distance of approximately  $r = 1500$  m. However, with growing energy of the CR, the distance at which the drop begins increases.

For SSDs, the amplitude of the asymmetry  $\alpha_\mu$  for the muonic component is also close to zero for small distances. However, in contrast to WCDs, the signals become very noisy with increasing distance. The higher the energy of the primary CR, the larger the distance to which signals are measured in a detector station.

### 4.3.3. Total Amplitude

The total amplitude of the asymmetry is composed of the amplitude of its sub-components: the electromagnetic and the muonic component. The normalized amplitude of the asym-

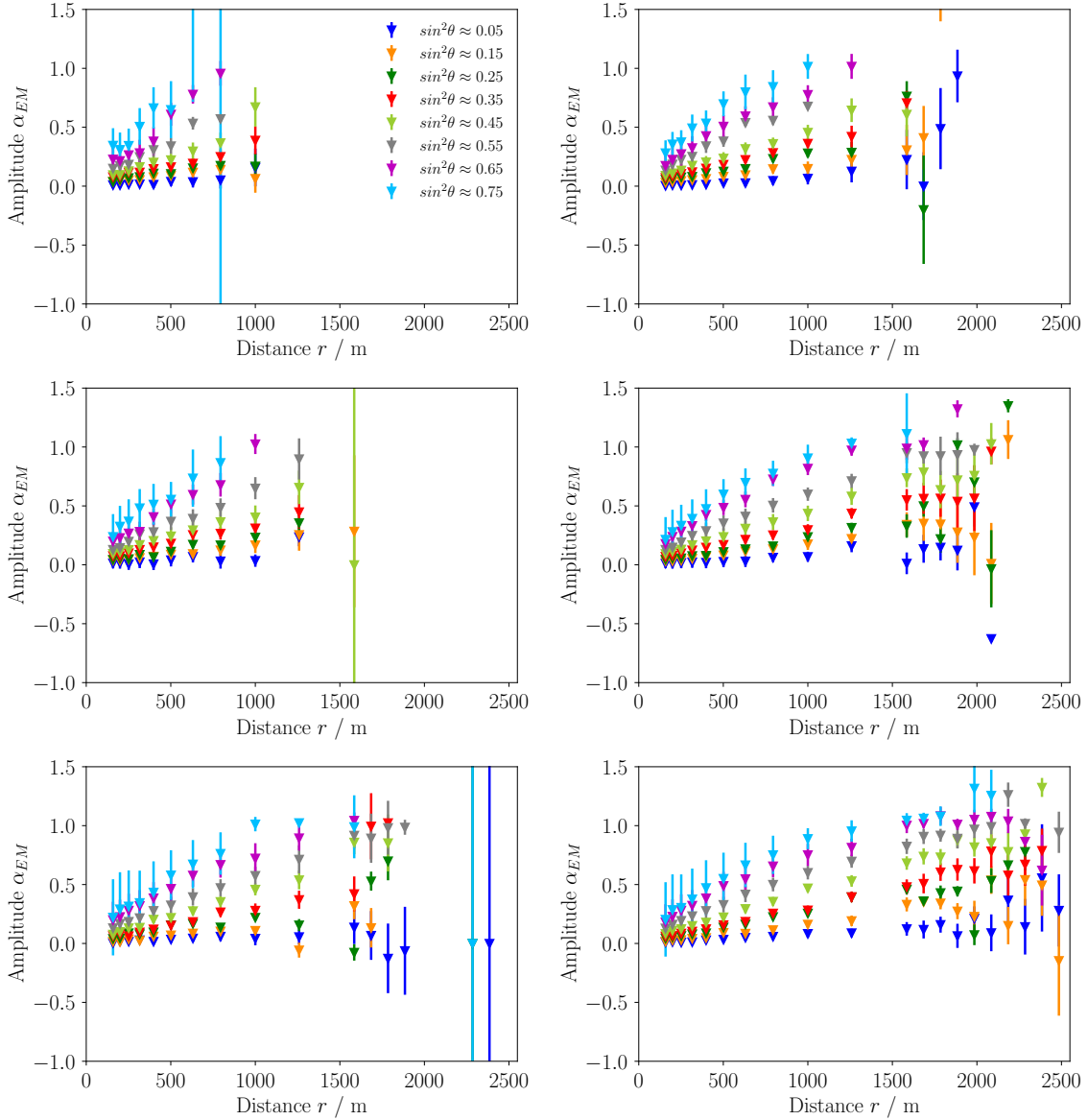


**Figure 4.6.:** Amplitude of the asymmetry  $\alpha_{EM}$  as a function of the distance from the shower axis for the electromagnetic component. From top to bottom the energies of the primary are  $18.5 < \lg(E/\text{eV}) < 18.6$ ,  $19.0 < \lg(E/\text{eV}) < 19.1$  and  $19.5 < \lg(E/\text{eV}) < 19.6$ . *Left:* Amplitude of the asymmetry  $\alpha_{EM}$  for SSDs. *Right:* Amplitude of the asymmetry  $\alpha_{EM}$  for WCDs.

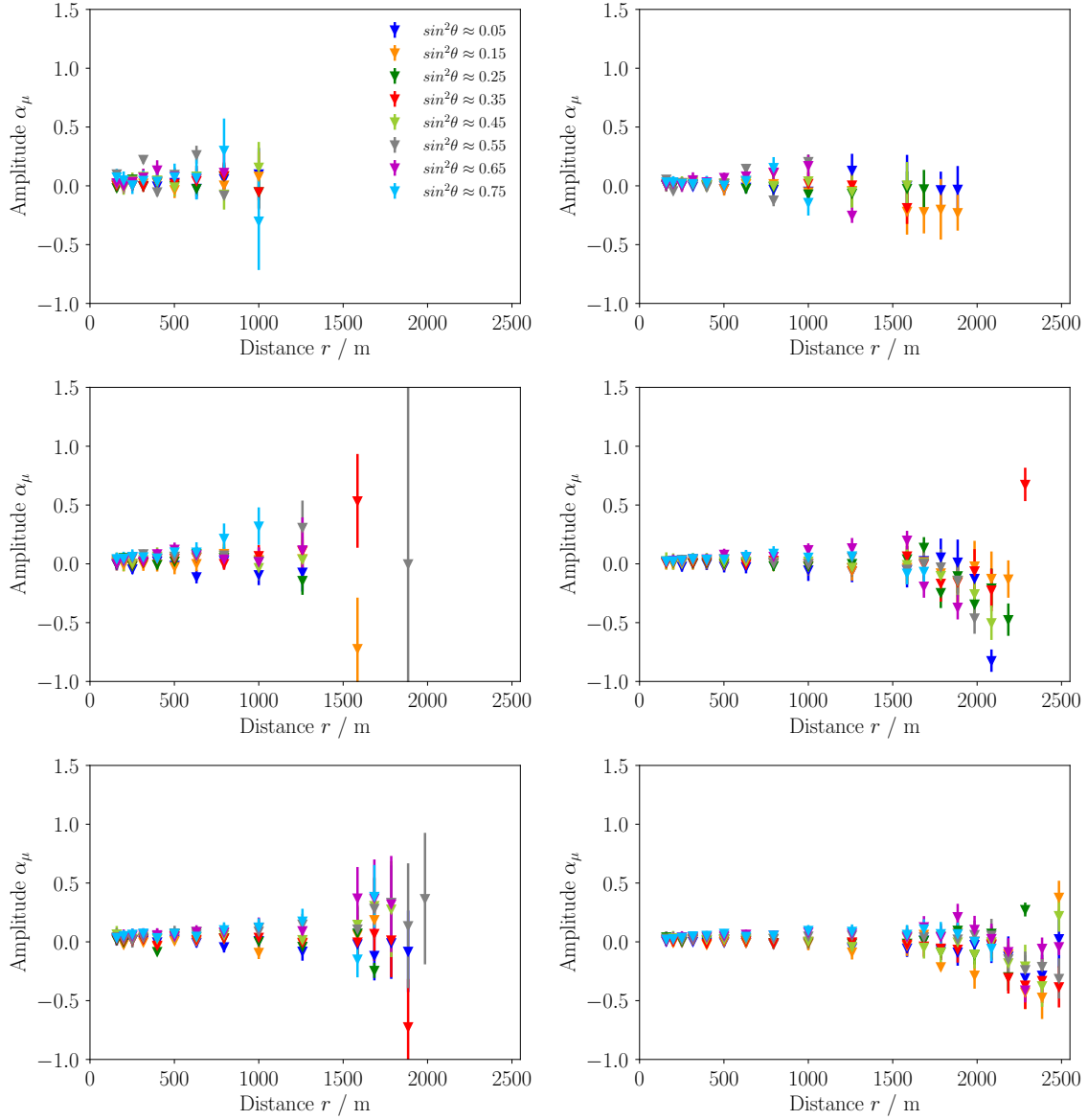


**Figure 4.7.:** Amplitude of the asymmetry  $\alpha_\mu$  as a function of the distance from the shower axis for the muonic component. From top to bottom the energies of the primary are  $18.5 < \lg(E/\text{eV}) < 18.6$ ,  $19.0 < \lg(E/\text{eV}) < 19.1$  and  $19.5 < \lg(E/\text{eV}) < 19.6$ . *Left:* Amplitude of the asymmetry  $\alpha_\mu$  for SSDs. *Right:* Amplitude of the asymmetry  $\alpha_\mu$  for WCDs.

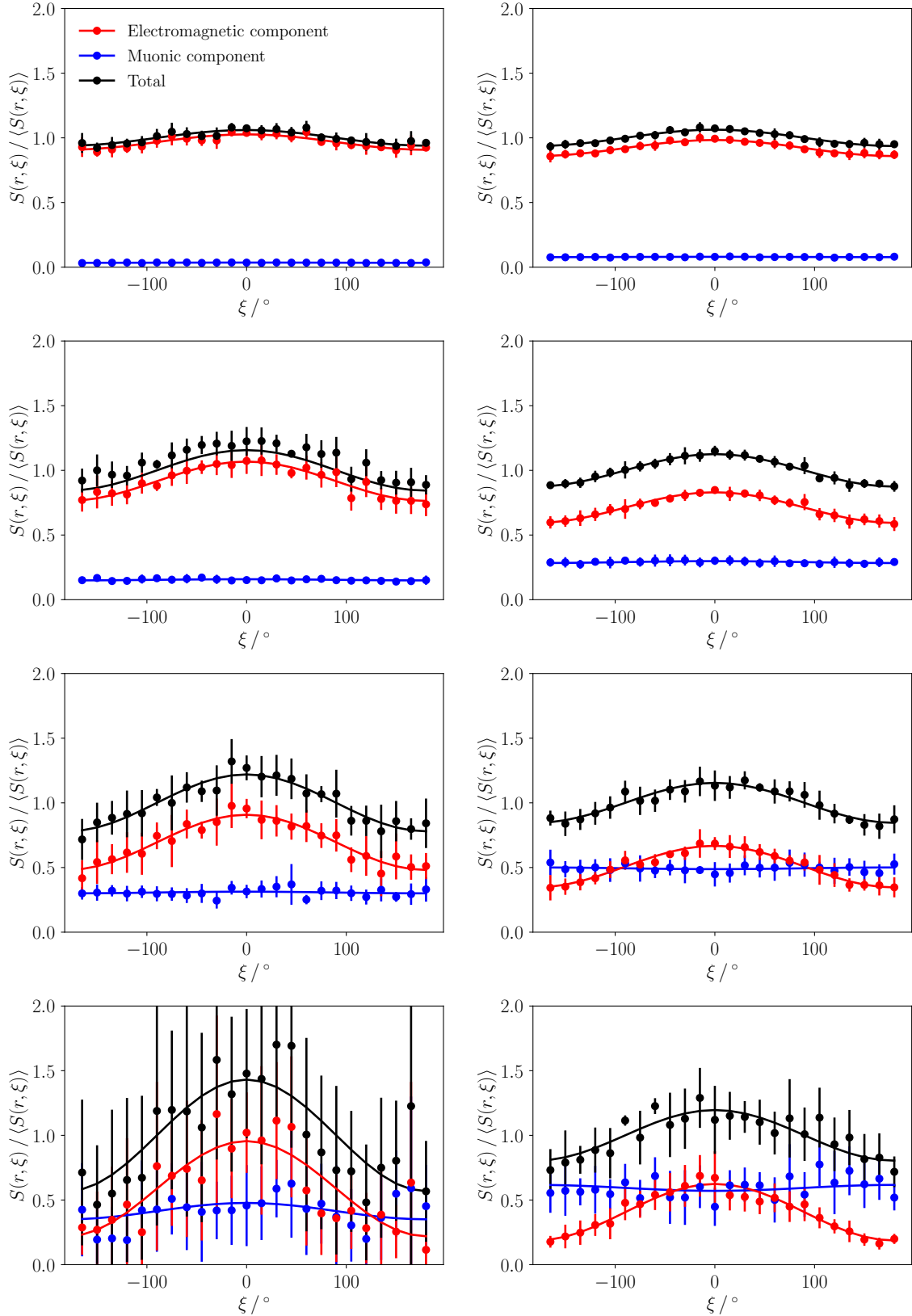


**Figure 4.8.:** The amplitude of the asymmetry for the different non-saturated shower components. The total unsaturated signal (black) consists of the sum of the electromagnetic component (red) and the muonic component (blue). From top to bottom, the distances are  $r = 158$  m, 501 m, 1000 m and 1584 m. The shown distributions use simulated showers which are generated by a proton primary with energies between  $19.4 < \lg(E/\text{eV}) < 19.5$  and with zenith angles between  $0.3 < \sin^2 \theta < 0.4$ . *Left:* Signals measured with SSDs. *Right:* Signals measured with WCDs.

metry for the different shower components are plotted together in Figure 4.8. The signals measured with SSDs are shown on the left, while the signals measured with WCDs are shown on the right. By comparing the plots for SSDs and WCDs, it is noticeable that each detector emphasizes the shower components in different ways, dependent on the distance to the shower axis. These differences are due to the different shapes of the detectors and their different responses depending on the particles they pass through. The amplitude of the asymmetry in SSDs is mainly driven by the electromagnetic component, independent of the distance from the shower axis. WCDs are sensitive to both, electromagnetic and muonic components. The balance of the components in the total signal is strongly dependent on the distance. The contribution of the electromagnetic component to the total amplitude is predominant near the shower axis and decreases with distance. In contrast, the muonic component increasingly dominates the behavior of the total amplitude, the higher the distance to the shower axis. This is explained by the fact, that at large distances, the electromagnetic component has largely been absorbed in the atmosphere. Therefore, the distribution at large distances is dominated by muons.

At small distances, the total amplitude of the asymmetry for SSDs and WCDs looks approximately the same. Both total amplitudes are mainly driven by the electromagnetic shower component and are affected by the geometrical and attenuation effects almost the same way, resulting in a nearly equal value for the total amplitude of the asymmetry. With the progressive absorption of the electromagnetic shower component when increasing the distance from the shower axis, the contribution from the muonic component to the total amplitude increases. Compared to SSDs, WCDs are more sensitive to the muonic component at high distances. As observed in Figure 4.7, the muonic component is around zero for small distances and is decreasing for large distances. The dominance of muons in the distribution for WCDs, therefore, flattens the total amplitude of the asymmetry at large distances. The total amplitude of the asymmetry for SSDs is still determined by the electromagnetic component. Hence, for SSDs, the azimuthal asymmetry is larger. Since the accuracy of the signal measurement decreases at large distances due to progressive absorption, noisy behavior and increasing uncertainties are observed, especially for SSDs. From the data received from SSDs, an estimator of the electromagnetic component is obtained. By subtracting the electromagnetic component from the total signal measured in WCDs, the muonic component is estimated.

#### 4.4. Correction of the Asymmetry

The objective of this thesis is the correction of the bias introduced by the azimuthal asymmetry in signals measured with SSDs and WCDs. To develop an appropriate model, many fitting processes must be carried out. The amplitude of the asymmetry is strongly dependent on the distance  $r$ , the zenith angle  $\theta$  and to a lower extent on the energy  $E$ . These dependencies must be considered to obtain a suitable model. Two different approaches are used to develop the model. The first path considers distance dependence first, while the second path considers zenith angle dependence first. Both paths result in the same model. Deriving a model in two different ways offers the possibility to identify possible outliers or problems with the parametrization.

##### 4.4.1. Dependency on Distance

After the shower components have been considered in detail, the total amplitude of the asymmetry  $\alpha$  is plotted as a function of the distance  $r$ . The amplitude of the asymmetry as a function of the distance for three different energies, for both WCDs and SSDs, is depicted in Figure 4.9. For WCDs, the amplitude of the asymmetry  $\alpha$  increases from 0 to  $\sim 500$  m. Then, the distribution remains constant before it drops to negative values. The decrease starts at about  $\sim 1500$  m, but the exact value depends on the energy of the primary particle. The higher the energy of the CR, the greater is the distance at which the drop begins.

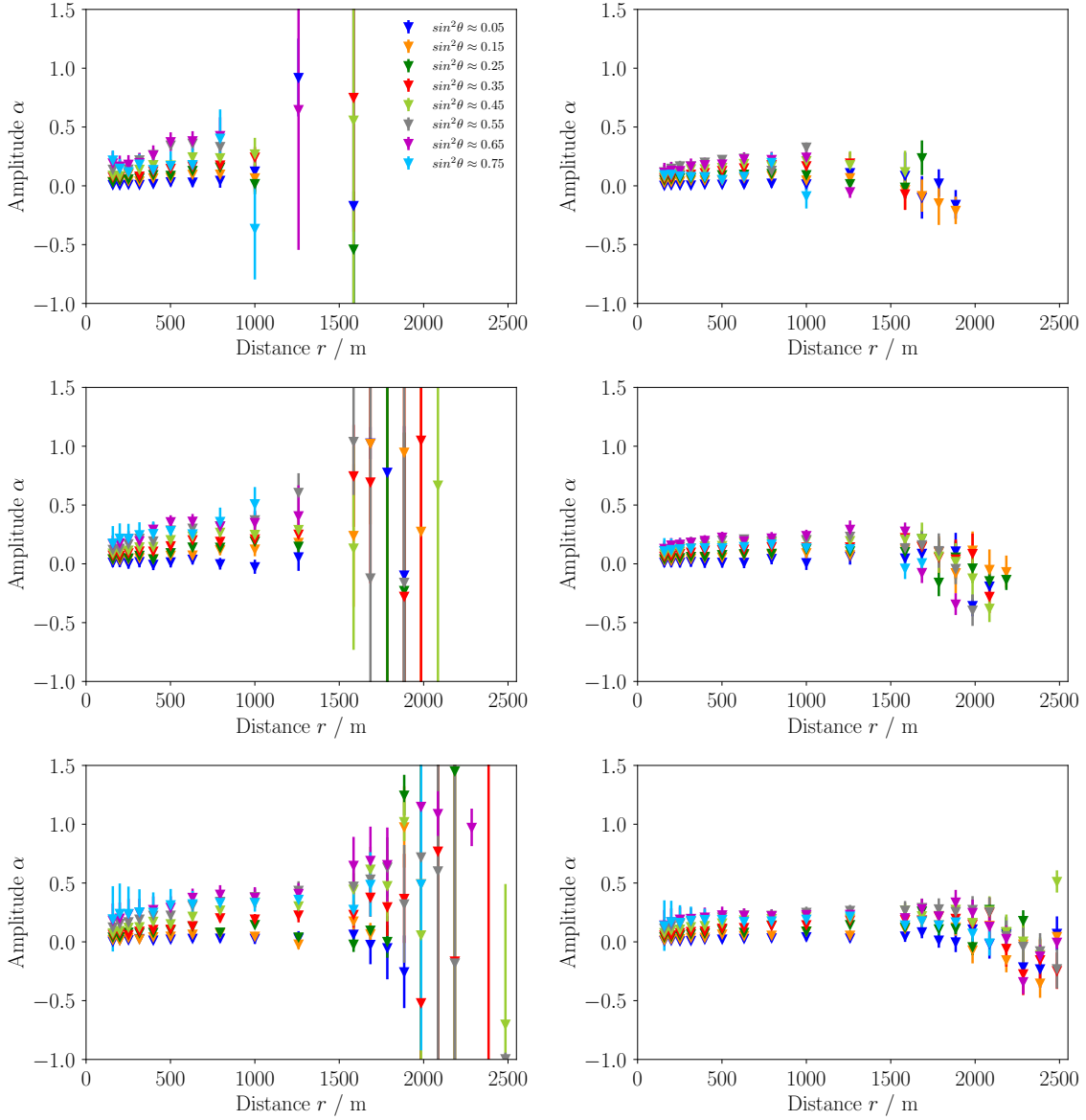


**Figure 4.9.:** Total amplitude of the asymmetry  $\alpha$  as a function of the distance  $r$  from the shower axis for different zenith angles  $\theta$  and for different energies of the primary. From top to bottom the energies are  $18.5 < \lg(E/\text{eV}) < 18.6$ ,  $19.0 < \lg(E/\text{eV}) < 19.1$  and  $19.5 < \lg(E/\text{eV}) < 19.6$ . *Left:* Amplitude of the asymmetry  $\alpha$  for SSDs. *Right:* Amplitude  $\alpha$  of the asymmetry for WCDs.

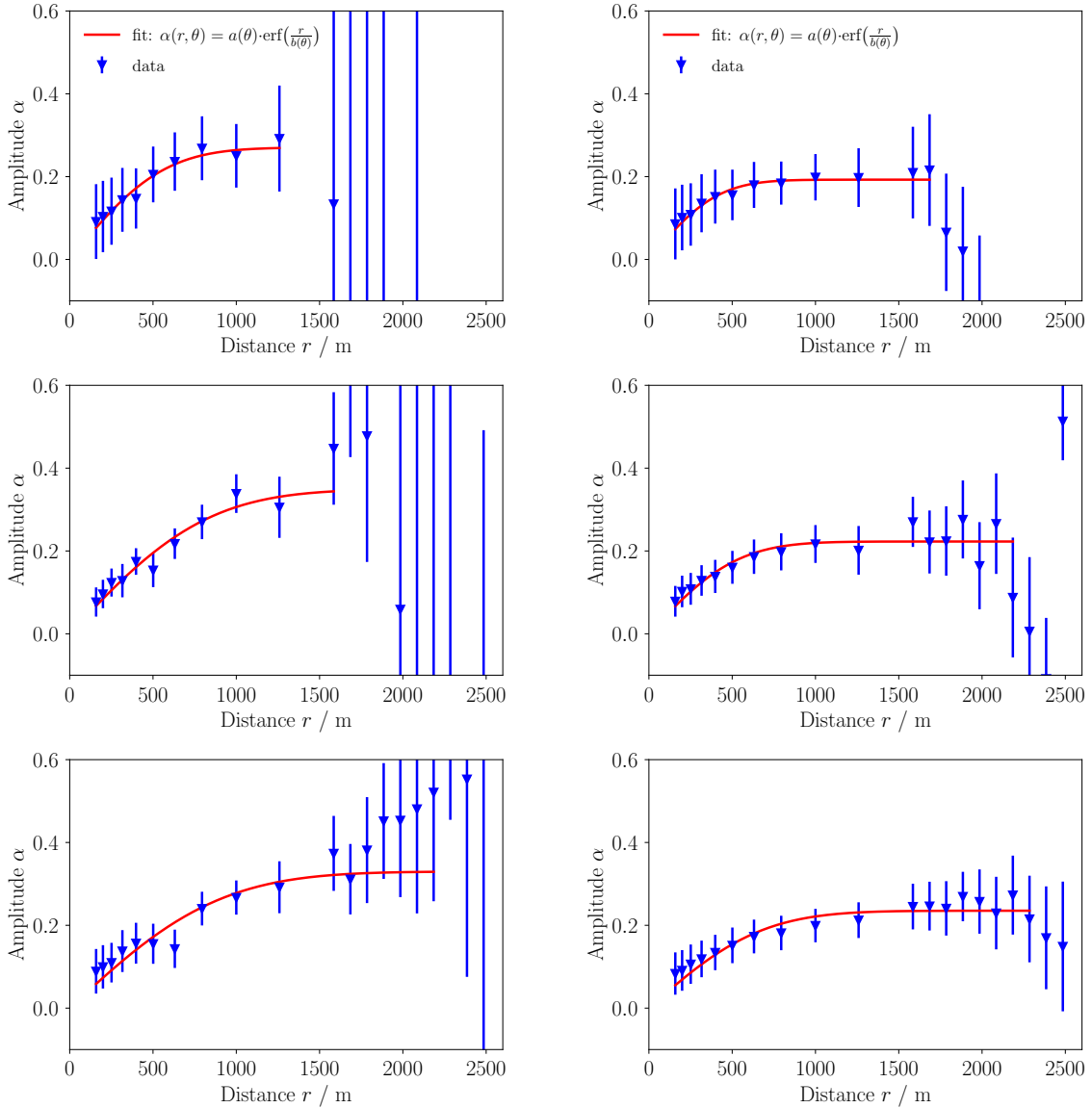


**Figure 4.10.:** Fit of the total amplitude of the asymmetry  $\alpha$  as a function of the distance  $r$  from the shower axis for  $\sin^2 \theta \approx 0.45$  and for different energies of the primary. From top to bottom the energies are  $19.0 < \lg(E/\text{eV}) < 19.1$ ,  $19.5 < \lg(E/\text{eV}) < 19.6$  and  $19.9 < \lg(E/\text{eV}) < 20.0$ . *Left:* Fit for SSDs. The noisy signals at large distances are not considered in the fitting procedure. *Right:* Fit for WCDs. The decrease of the amplitude at large distances is not considered in the fitting procedure.

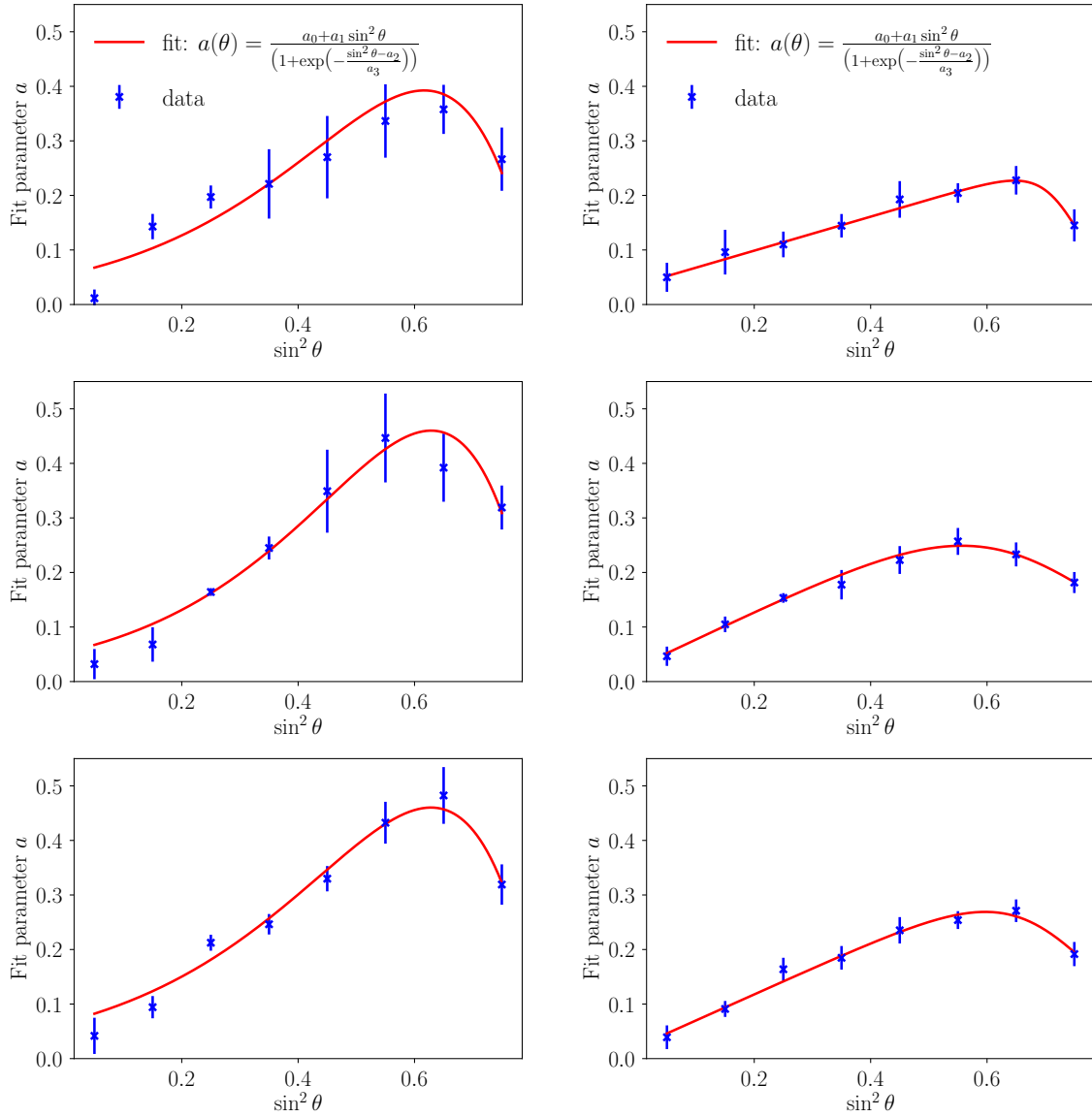


**Figure 4.11.:** Fit of the fit parameter  $a$  as a function of  $\sin^2 \theta$  for different energies of the primary. From top to bottom the energies are  $19.0 < \lg(E/\text{eV}) < 19.1$ ,  $19.5 < \lg(E/\text{eV}) < 19.6$  and  $19.9 < \lg(E/\text{eV}) < 20.0$ . *Left:* Fit for SSDs. *Right:* Fit for WCDs.

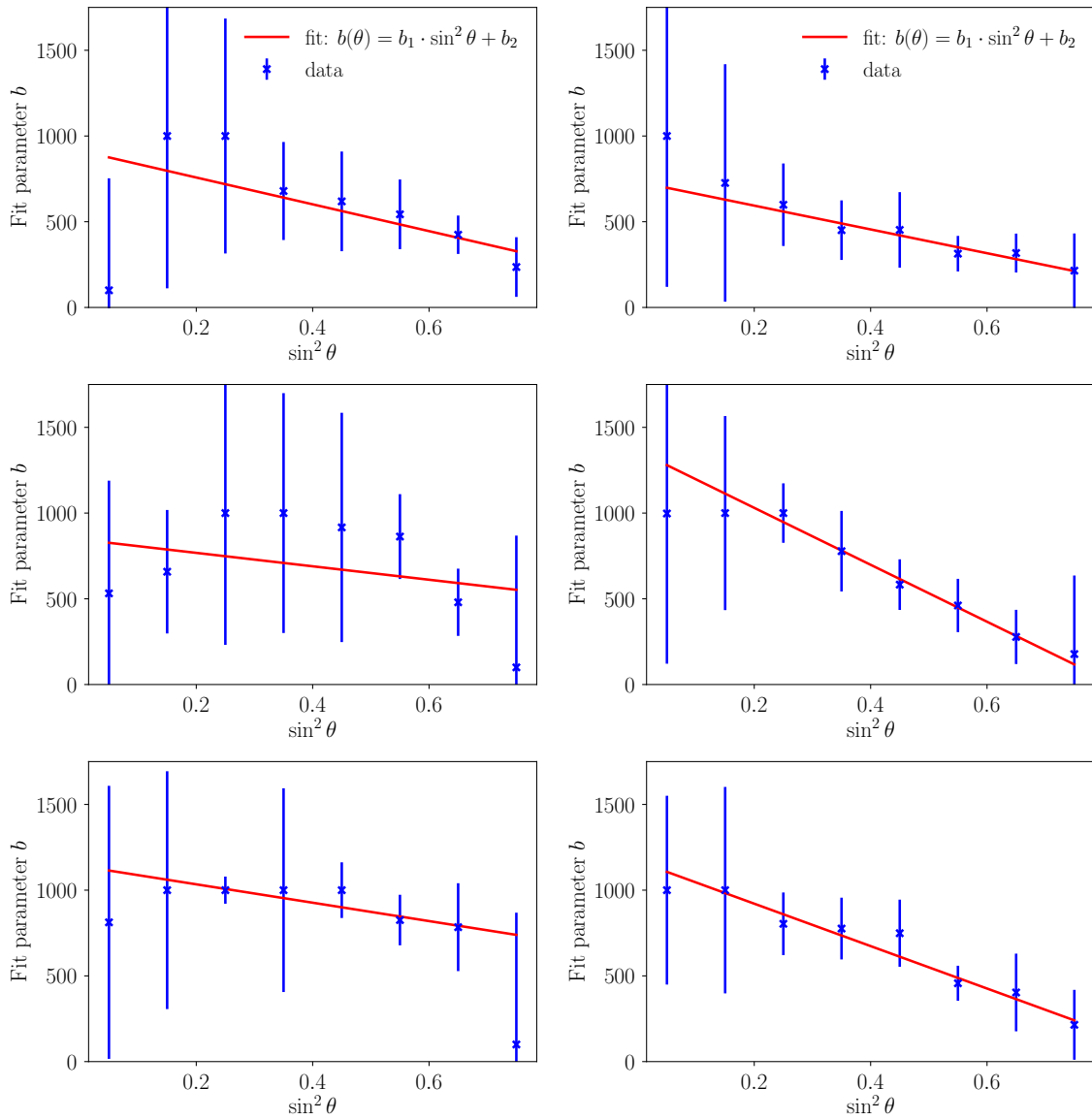


**Figure 4.12.:** Fit of the fit parameter  $b$  as a function of  $\sin^2\theta$  for different energies of the primary. From top to bottom the energies are  $19.0 < \lg(E/\text{eV}) < 19.1$ ,  $19.5 < \lg(E/\text{eV}) < 19.6$  and  $19.9 < \lg(E/\text{eV}) < 20.0$ . *Left:* Fit for SSDs. *Right:* Fit for WCDs.

At small distances, the amplitude of asymmetry is driven by the electromagnetic shower component. With growing distance, the absorption of the electromagnetic component increases. For this reason, the total signal at large distances from the shower axis is dominated by muons, which leads to a decrease of the amplitude of the asymmetry.

The amplitude  $\alpha$  largely depends on the zenith angle  $\theta$ . An air shower with a low inclination ( $\sin^2 \theta \approx 0.05$ ), has an amplitude of the asymmetry close to zero. Up to a zenith angle of  $\sin^2 \theta \approx 0.65$ , the amplitude of the asymmetry increases with the inclination of the shower. For more inclined zenith angles ( $\sin^2 \theta \approx 0.75$ ), however, the amplitude of the asymmetry reduces. This observation is consistent with the hypothesis formulated in Section 4.1.1, which states that showers with a large zenith angle are dominated by muons, implying lower values of the asymmetry. It seems, that the decrease due to muons occurs only above a zenith angle which is about  $\sin^2 \theta \approx 0.65$ .

For SSDs, the amplitude of the asymmetry also increases up to  $\sim 500$  m, before arriving at a plateau. The amplitude of the asymmetry remains constant until a distance of  $\sim 1500$  m is reached. With a lower energy of the primary particle, the plateau already ends at shorter distances. Unlike WCDs, the amplitude for SSDs does not start to decrease after the end of the plateau. Since the amplitude of the asymmetry for SSDs is mainly caused by the electromagnetic shower component, no decrease of the amplitude is observed at large distances. Instead, the signals become very noisy for distances above  $\sim 1500$  m, due to the progressive absorption. Starting at approximately the same value of the amplitude for SSDs and WCDs, the amplitude of the asymmetry for SSDs takes greater values than WCDs at longer distances. The amplitude of the asymmetry is almost twice as high for SSDs than for WCDs. At short distances, the total amplitude of both detectors is dominated by the electromagnetic component to a large extent. At long distances, the total amplitude of the asymmetry for SSDs is mainly driven by the electromagnetic component, while the total amplitude for WCDs consists mainly of the muonic component.

To derive a parametrization of the amplitude, a model function must be found, which describes the data best. Since the energy dependence of the amplitude is assumed to be a second-order effect, the fit is initially applied only to primary particles with energies of  $19.9 < \lg(E/\text{eV}) < 20.0$ . On the basis of an empirical investigation, the fitting function

$$\alpha(r, \theta) = a(\theta) \cdot \operatorname{erf} \left( \frac{r}{b(\theta)} \right) \quad (4.9)$$

is selected, for both SSDs and WCDs. Since the performed fitting is very sensitive, it is necessary to set limits for the fitting parameters. Another difficulty is, that it is numerically possible to obtain different sets of parameters that allow a “good fit”. For these reasons, some parameters must be constrained. The parameter  $b(\theta)$  is empirically chosen to be constrained between  $b(\theta) = [100, 1000]$  m. This interval prevents divergence of the fit and underestimation of the amplitude near the core. Since the values for the minimization process are given with their associated errors, the points are weighted according to their errors during the fitting process.

Figure 4.10 depicts examples for  $\sin^2 \theta \approx 0.45$  and for three different energies:  $19.0 < \lg(E/\text{eV}) < 19.1$ ,  $19.5 < \lg(E/\text{eV}) < 19.6$  and  $19.9 < \lg(E/\text{eV}) < 20.0$ . The data is shown with the best fitted results for Eq. 4.9, which is indicated by the red line.

For WCDs-right panels, the amplitude of the asymmetry decreases with larger distances, due to the dominance of muons. The derived model does not take this decrease into account. To simplify the model and to restrain the numbers of fitted parameters, it is assumed that the amplitude of asymmetry is constant at  $\alpha(1500)$  for distances above  $r = 1500$  m. For SSDs-left panels, the noisy signal is not considered and the amplitude is also assumed to be constant at large distances. Fitting the data provides a value for the parameters  $a(\theta)$  and  $b(\theta)$ , for each bin in zenith angle and energy. As a next step, the two fit parameters are plotted as a function of  $\sin^2 \theta$ .

**Table 4.2.:** Fit parameters for WCDs and SSDs averaged over all energies.

Fit parameter	WCD	SSD
$a_0$	0.0219	18
$a_1$	0.423	-22
$a_2$	0.733	0.983
$a_3$	-0.0812	0.170
$b_1/m$	-988	-840
$b_2/m$	931	1082

Figure 4.11 depicts the fit parameter  $a(\theta)$  as a function of  $\sin^2 \theta$  for SSDs-left panels and WCDs-right panels. From top to bottom the energies are  $19.0 < \lg(E/\text{eV}) < 19.1$ ,  $19.5 < \lg(E/\text{eV}) < 19.6$  and  $19.9 < \lg(E/\text{eV}) < 20.0$ . With this distributions, another curve fitting process is performed. The empirically selected fit function is

$$a(\theta) = \frac{a_0 + a_1 \sin^2 \theta}{\left(1 + \exp\left(-\frac{\sin^2 \theta - a_2}{a_3}\right)\right)}. \quad (4.10)$$

Like before, constraints are needed to make the fit converging. These constraints are also determined empirically. For SSDs, a constraint on the fit parameter  $a_{0,\text{SSD}} = [15, 25]$  is used. For WCDs, no constraints on the fitting parameters are needed. The distribution of the fit parameter  $a(\theta)$  as a function of  $\sin^2 \theta$  initially increases for both detectors, before reaching a maximum value at  $\sin^2 \theta \approx 0.65$  and then decreases. By comparing SSDs to WCDs, it is noticeable that the maximal value for SSDs is higher than for WCDs. Additionally, an exponential increase takes place for SSDs, while WCDs increases linearly.

Likewise, the fit parameter  $b(\theta)$  is plotted as a function of  $\sin^2 \theta$ . Examples of this distribution are shown in Figure 4.12 for three different energies:  $19.0 < \lg(E/\text{eV}) < 19.1$ ,  $19.5 < \lg(E/\text{eV}) < 19.6$  and  $19.9 < \lg(E/\text{eV}) < 20.0$ . Due to the large uncertainties and the approximately linear behavior for SSDs-left panels and WCDs-right panels, the distributions are fitted with a linear function

$$b(\theta) = b_1 \cdot \sin^2 \theta + b_2. \quad (4.11)$$

The parameters of the fit functions  $a(\theta)$  and  $b(\theta)$  are calculated in each range in energy and are listed in Appendix A. By averaging the fitting results over all energies, the values shown in Table 4.2 are finally obtained.

#### 4.4.2. Dependency on Zenith Angle

The second approach to derive the described model, considers the dependence on the zenith angle  $\theta$  first. The total amplitude of the asymmetry  $\alpha$  as a function of  $\sin^2 \theta$  is illustrated in Figure 4.13, for both SSDs-left panels and WCDs-right panels. The amplitude is depicted at four different distances  $r$  from the shower axis: 158.5 m (blue), 501.2 m (orange), 1000 m (green) and 1584.9 m (red). For WCDs, the total amplitude of the asymmetry is zero for non-inclined showers and increases almost linearly until  $\sin^2 \theta \approx 0.55$  is reached. After the peak of  $\sim 0.25$ , the distribution decreases to  $\sim 0.15$ , for  $r = 1000$  m.

A similar behavior is observed for SSDs. Unlike WCD, the distribution at low zenith angles does not increase linearly, but exponentially. The maximum turning point of this distribution is located at  $\sin^2 \theta \approx 0.65$ . Compared to the distribution for WCDs, the amplitude of the asymmetry is higher. Starting at approximately zero for vertically

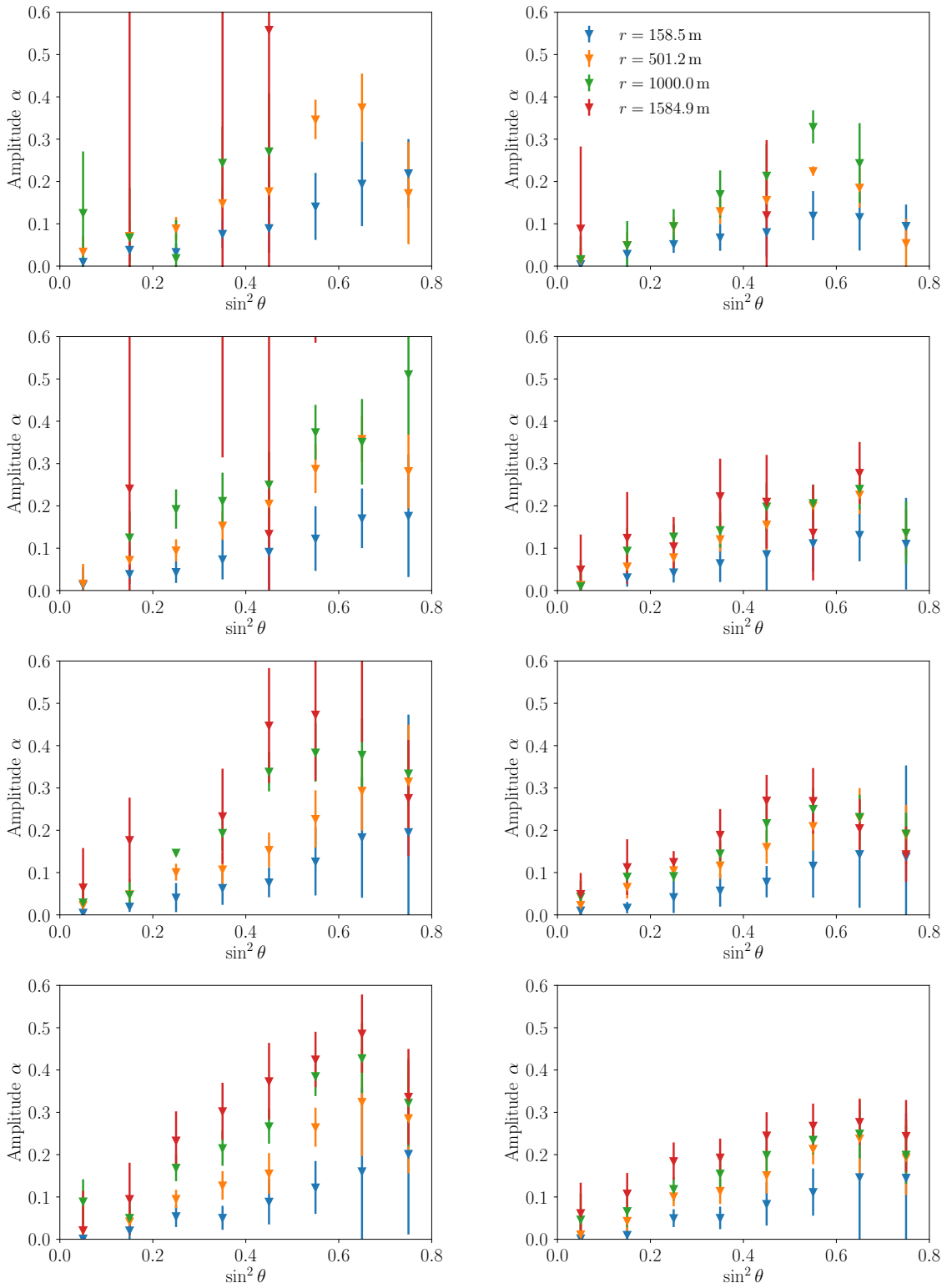


**Figure 4.13:** Total amplitude of the asymmetry  $\alpha$  as a function of  $\sin^2 \theta$  for different distances  $r$  and for different energies of the primary. From top to bottom the energies are  $18.5 < \lg(E/\text{eV}) < 18.6$ ,  $19.0 < \lg(E/\text{eV}) < 19.1$ ,  $19.5 < \lg(E/\text{eV}) < 19.6$  and  $19.9 < \lg(E/\text{eV}) < 20.0$ . *Left:* Amplitude of the asymmetry for SSDs. *Right:* Amplitude of the asymmetry for WCDs.

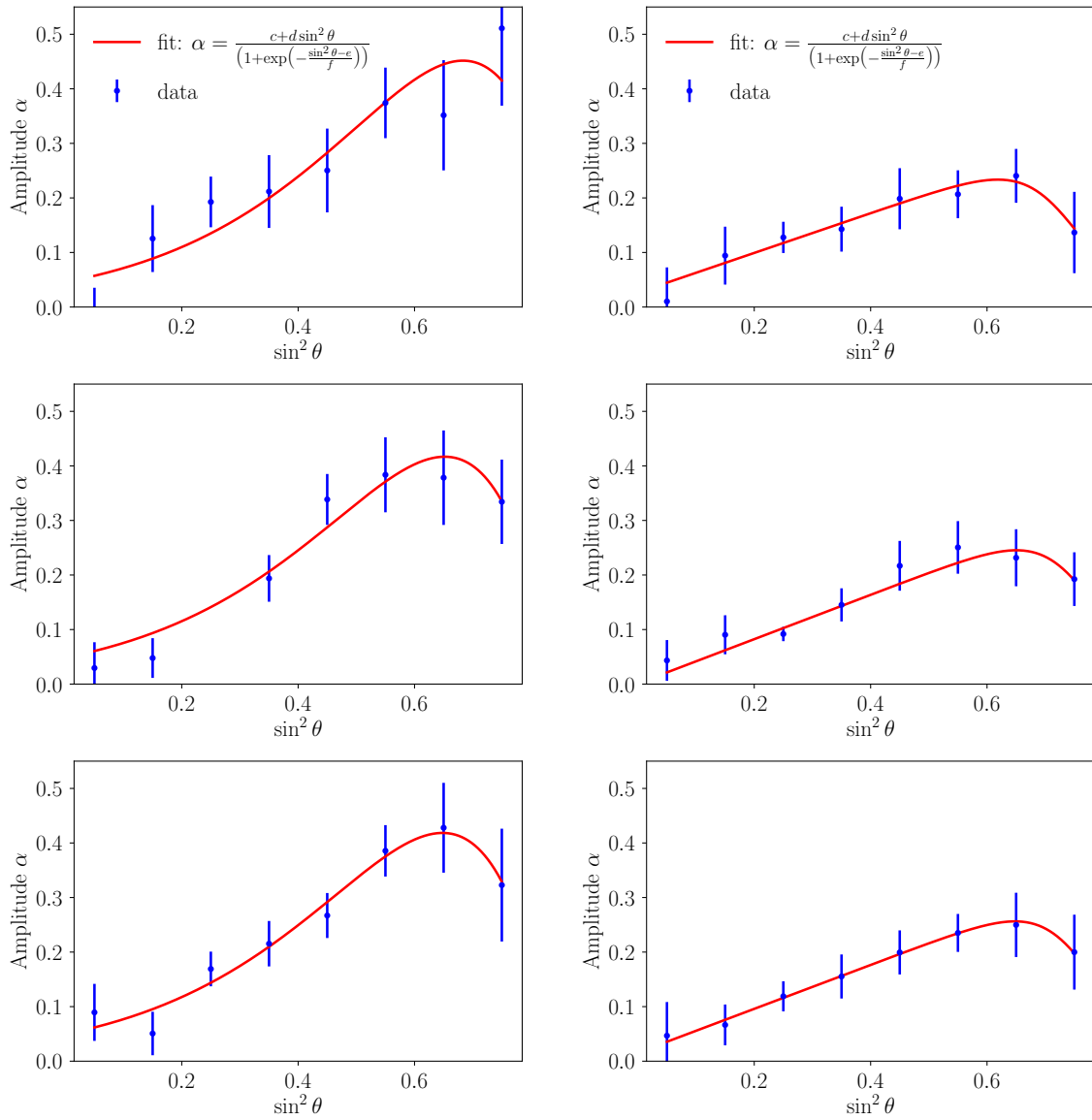


**Figure 4.14.:** Fit of the total amplitude of the asymmetry  $\alpha$  as a function of  $\sin^2 \theta$  for  $r = 1000$  m and for different energies of the primary. From top to bottom the energies are  $19.0 < \lg(E/\text{eV}) < 19.1$ ,  $19.5 < \lg(E/\text{eV}) < 19.6$  and  $19.9 < \lg(E/\text{eV}) < 20.0$ . *Left:* Fit for SSDs. *Right:* Fit for WCDs.

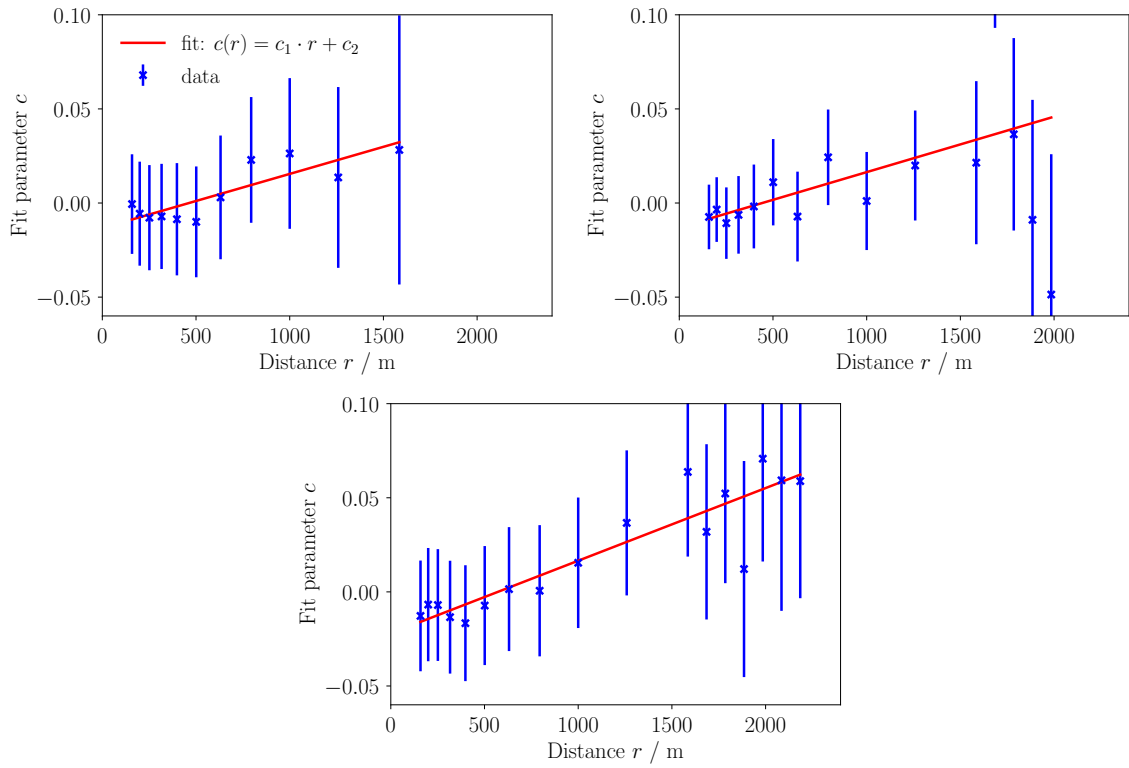


**Figure 4.15.:** Fit of the fit parameter  $c$  for WCDs as a function of the distance  $r$  for different energies of the primary. The energies are  $19.0 < \lg(E/\text{eV}) < 19.1$  (*top-left*),  $19.5 < \lg(E/\text{eV}) < 19.6$  (*top-right*) and  $19.9 < \lg(E/\text{eV}) < 20.0$  (*bottom*).

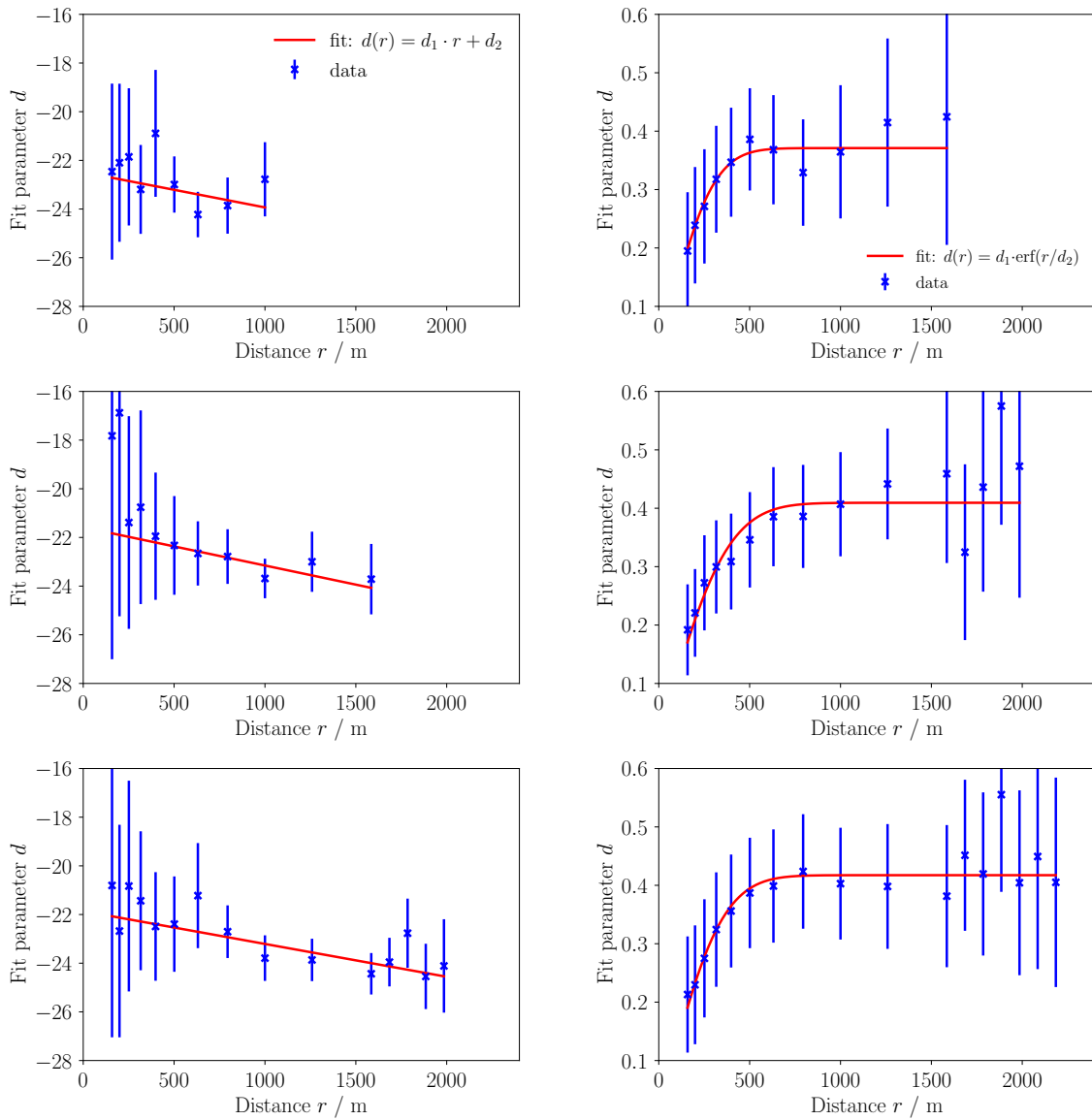


**Figure 4.16.:** Fit of the fit parameter  $d$  as a function of the distance  $r$  for different energies of the primary. From top to bottom the energies are  $19.0 < \lg(E/\text{eV}) < 19.1$ ,  $19.5 < \lg(E/\text{eV}) < 19.6$  and  $19.9 < \lg(E/\text{eV}) < 20.0$ . *Left:* Fit for SSDs. *Right:* Fit for WCDs.

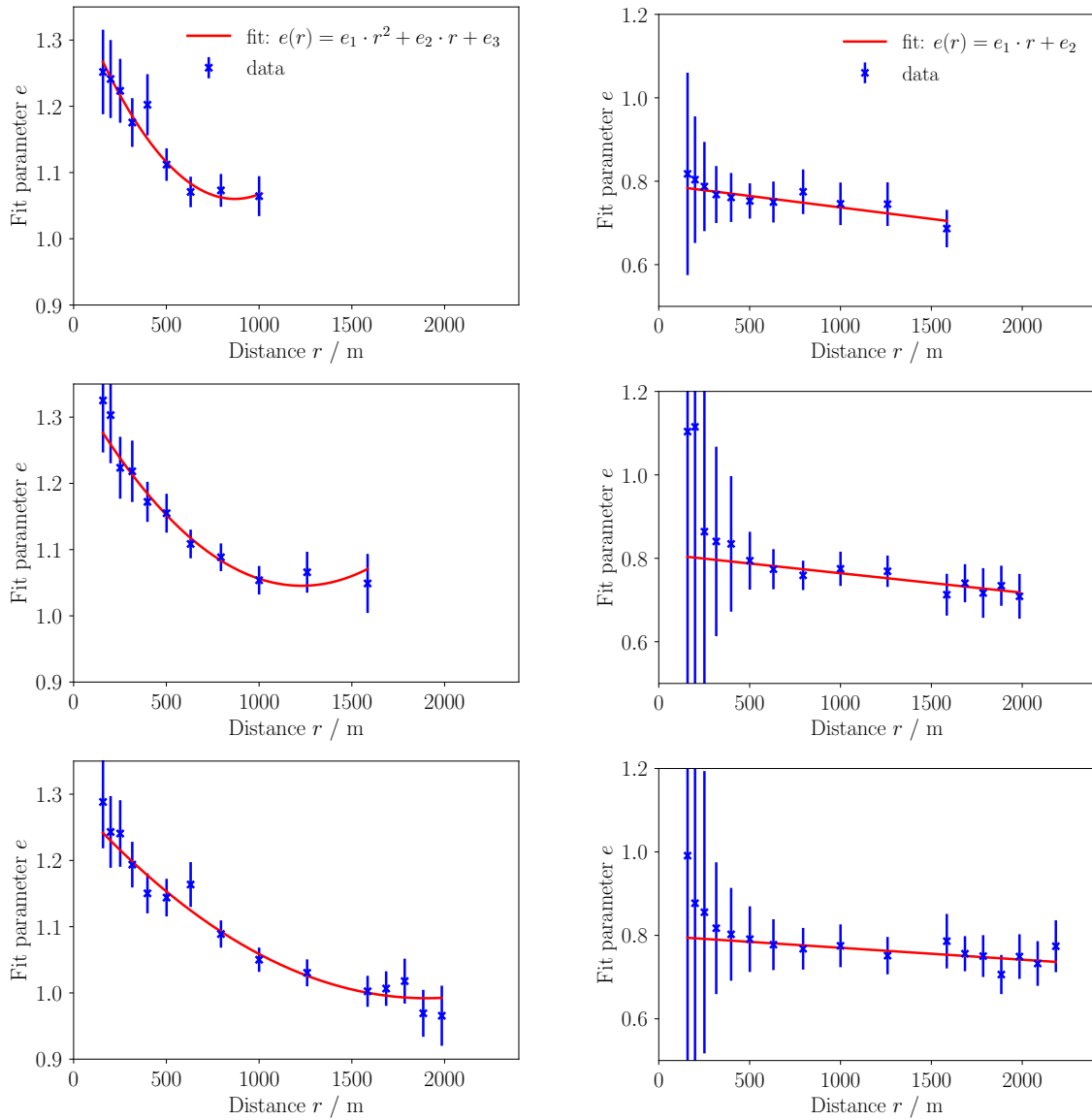


**Figure 4.17.:** Fit of the fit parameter  $e$  as a function of the distance  $r$  for different energies of the primary. From top to bottom the energies are  $19.0 < \lg(E/\text{eV}) < 19.1$ ,  $19.5 < \lg(E/\text{eV}) < 19.6$  and  $19.9 < \lg(E/\text{eV}) < 20.0$ . *Left:* Fit for SSDs. *Right:* Fit for WCDs.

incoming showers, the distribution reaches  $\sim 0.4$  and drops to  $\sim 0.35$ , for  $r = 1000$  m. The distribution of the amplitude of asymmetry as a function of the zenith angle is consistent with the hypotheses formulated in Section 4.1.1 and 4.1.2. At small zenith angles, the geometric effect dominates the distribution of the asymmetry, leading to an increase in the amplitude of the asymmetry. With growing zenith angle, the contribution of the attenuation effect increases. The observed decrease of the amplitude at zenith angles above  $\sin^2 \theta \approx 0.65$  is due to the muon dominance of the shower at ground level. As a consequence of the long distance through the atmosphere, the electromagnetic component gets progressively absorbed. Since no asymmetry occurs for muons, the total amplitude of the asymmetry decreases. Furthermore, the plotted data confirms that no asymmetry occurs at zenith angles equal to zero.

With growing distance from the shower axis, the amplitude of the asymmetry increases. At low energies only the stations close to the shower axis report a trigger. This is observed in Figure 4.13-top for SSDs-left panel and WCDs-right panel at a distance of  $r = 1584.9$  m.

Many data points are missing because no signals were recorded. The few data points that are displayed have large uncertainties. With growing energy of the CR, the signals are increasingly recorded in stations of greater distance.

In search for the best adjustment of the data, the model function

$$\alpha(r, \theta) = \frac{c(r) + d(r) \sin^2 \theta}{\left(1 + \exp\left(-\frac{\sin^2 \theta - e(r)}{f(r)}\right)\right)}, \quad (4.12)$$

is chosen fully empirical, for both SSDs and WCDs. Due to the strong correlation of the fitting parameters, constraints on the parameters are required and some parameters need to be fixed. Fitting the distribution for WCDs without any constraints, provides an approximately constant behavior of the fit parameter  $f_{\text{WCD}}$  around  $\sim -0.05$ . Hence,  $f_{\text{WCD}}$  is set to  $-0.05$ . With this restriction, the fit is performed without constraining any of the other parameters.

The fit for the SSDs is performed in the same way. Performing the fit without any restrictions leads to the parameter  $f_{\text{SSD}}$  fixed at  $f_{\text{SSD}} = 0.175$ . Since the total amplitude of the asymmetry for SSDs has larger values than the amplitude for WCDs, it makes physical sense that the absolute value of  $f_{\text{WCD}}$  is smaller than the value of  $f_{\text{SSD}}$ . At Eq. 4.12 it is noticeable, that  $f(r)$  is written in the denominator of an exponential function. The exponential function itself is also in the denominator. The smaller the value in the denominator, the larger the value of the fraction. A smaller absolute value for  $f_{\text{WCD}}$ , therefore, results in a smaller value of the amplitude for WCDs. For SSDs in contrast, a greater absolute value of  $f_{\text{SSD}}$  results in a greater value of the amplitude of asymmetry.

After the parameter  $f_{\text{SSD}}$  has been constrained, the fit process is repeated. With the parameter  $f_{\text{SSD}}$  being fixed, the fit parameter  $c_{\text{SSD}}$  as a function of the distance behaves approximately constant around  $\sim 20$ . Consequently, the fit parameter is set to be  $c_{\text{SSD}} = 20$ . Examples of the fitting, performed with the found boundary conditions for a distance at  $r = 1000$  m from the shower axis, are shown in Figure 4.14 for SSDs-left panels and WCDs-right panels.

A comparison with the distribution of the fit parameter  $a(\theta)$  a function of  $\sin^2 \theta$  in Figure 4.11 illustrates that the two approaches of deriving the model, result in similar behavior. Eq. 4.10 is easy to identify with Eq. 4.12. Therefore,  $a_0$  and  $a_3$  are identified with  $c(r)$  and  $f(r)$ , respectively. The parameter  $a_{0,\text{SSD}} = 18$  has a percentage deviation of 11.11% from the parameter  $c_{\text{SSD}}(r) = 20$ . For  $a_{3,\text{SSD}} = 0.170$  the percentage deviation to  $f_{\text{SSD}} = 0.175$  is 2.94%, while for  $a_{3,\text{WCD}} = -0.0812$  and  $f_{\text{WCD}} = -0.05$  a percentage difference of 38.42% exists. The parameters are compatible with each other within their respective uncertainties. The resulting parameters from the fit in Figure 4.14, are plotted as a function of the distance  $r$ . The fit parameter  $c_{\text{WCD}}(r)$  as a function of the distance  $r$  for WCDs is shown in Figure 4.15. The distribution is approximately described by a linear function

$$c_{\text{WCD}}(r) = c_1 \cdot r + c_2, \quad (4.13)$$

with positive slope. It is interesting to note, that  $c_{\text{SSD}}(r)$  is not constant around zero as expected, but changing with the distance. Up to a distance of  $r \approx 500$  m, the distribution is approximately centered around zero. For larger distances,  $c_{\text{WCD}}(r)$  increases almost linearly. For SSDs,  $c_{\text{SSD}} = 20$  is set. With these values for  $c(r)$ , the fit does not fulfill the condition  $\alpha(0) = 0$  and therefore the amplitude for vertically incident showers is not zero. This behavior contradicts the expectation. Nevertheless, there are possible explanations which could lead to this non-zero amplitude. For example the impact of the Earth's geomagnetic field could lead to such a behavior [49]. Charged particles, moving through the Earth's atmosphere, could be deflected by the Earth's magnetic field according to their charge. The lateral density in the shower plane could therefore be blurred, depending on the inclination

**Table 4.3.:** Fit parameters for WCDs averaged over all energies.

Fit parameter	WCD
$c_1/\text{m}^{-1}$	$3.43 \cdot 10^{-5}$
$c_2$	-0.0183
$d_1$	0.401
$d_2/\text{m}$	346
$e_1/\text{m}^{-1}$	$-6.81 \cdot 10^{-5}$
$e_2$	0.797

**Table 4.4.:** Fit parameters for SSDs averaged over all energies.

Fit parameter	SSD
$d_1/\text{m}^{-1}$	$-2.56 \cdot 10^{-3}$
$d_2$	-22
$e_1/\text{m}^{-2}$	$2.72 \cdot 10^{-7}$
$e_2/\text{m}^{-1}$	$-5.63 \cdot 10^{-4}$
$e_3$	1.35

of the EAS and the magnetic field strength. Uncertainties in measurements of the signals could also be one of the reasons. It is likely, that the reason for the non-zero amplitude is a combination of several effects.

The fit parameter  $d(r)$  as a function of the distance  $r$  is depicted in Figure 4.16. For WCDs-right panels, the plots illustrate the typical distribution of the error function. As a consequence, the empirically-based fit function is set to be

$$d_{\text{WCD}}(r) = d_1 \cdot \text{erf}\left(\frac{r}{d_2}\right). \quad (4.14)$$

For SSDs-left panels, the distribution follows a linear function

$$d_{\text{SSD}}(r) = d_1 \cdot r + d_2, \quad (4.15)$$

with a negative slope.

The fit parameter  $e(r)$  as a function of the distance  $r$  is illustrated in Figure 4.17. For WCDs-right panels, a linear function

$$e_{\text{WCD}}(r) = e_1 \cdot r + e_2, \quad (4.16)$$

is selected to fit the data. The distribution for SSDs-left panels, is following a second order polynomial

$$e_{\text{SSD}}(r) = e_1 \cdot r^2 + e_2 \cdot r + e_3. \quad (4.17)$$

The parameters  $x_{\text{SSD}/\text{WCD}}(r)$  of the fit functions are calculated in each range in energy and are shown in Appendix B. Averaging the fit parameters over all energies, leads to the results shown in Table 4.3 and 4.4 for WCDs and SSDs, respectively.

#### 4.4.3. Dependency on Energy

The derived models are checked for different energies, to ensure that the same results are also observed in other bins in energy. Performing this test in each range in energy shows that energy dependence appears to be a second order effect. Furthermore, due to the large uncertainties, it would not be possible to determine the energy dependence. The models for different energies are compatible with each other within their respective uncertainties. To reduce the uncertainties, a larger number of simulated events need to be considered. For this reasons, energy dependency is not taken into account.

## 4.5. Derived Model

Using the derived model for WCDs, the events are resimulated. For this purpose, the two modules *LDFFinderKG* and *ScintillatorLDFFinderKG* in the SdReconstruction part of the Offline framework are modified to implement the derived parametrization. Using a Gaussian likelihood for WCDs and a truncated Gaussian likelihood for SSDs, the expected signals are calculated and compared to the measured signals during the reconstruction process. Instead of using

$$S(r) = S(1000) \cdot f_{\text{LDF}}(r), \quad (4.18)$$

the expected signals have been modified following

$$S(r) = S(1000) \cdot f_{\text{LDF}}(r) \cdot (1 + \alpha(r, \theta) \cos(\xi)), \quad (4.19)$$

with the derived parametrization  $\alpha(r, \theta)$ . As a result, the measured signals remain unmodified, whereas the expected signals get degraded. This has the advantage, that the systematical uncertainties of the models only affect the expected signals. It is checked, how the application of the derived model impacts the reconstruction in the position of the shower core.

### 4.5.1. Impact on the Core Position

So far, the reconstruction of the core position in the Offline framework is performed using WCD data only. Hence, this thesis only focuses on the core bias and core resolution for WCDs. Figure 4.18-top depicts the total distance  $\Delta\rho = \sqrt{(\vec{r}_{\text{rec}} - \vec{r}_{\text{MC}})^2}$  between the reconstructed and simulated core position in the shower plane coordinate system, as a function of the shower size  $\lg(S(1000)/\text{VEM})$  and as a function of  $\sin^2\theta$ . The black and red dots show the mean of all events within a bin with its associated dispersion, for the data without correction and the corrected data, respectively. The total distance  $\Delta\rho$  decreases from  $\sim 100$  m to  $\sim 35$  m with increasing shower size. The implementation of the derived model decreases the bias on average by  $\sim 20$  to 25 m. The total distance  $\Delta\rho$  of the data without correction increases with zenith angle. Applying the correction results in a total distance which is approximately constant around  $\sim 35$  m and thus loses its dependency on the zenith angle. The more inclined the shower, the greater is the distance by which the correction is made.

The bias in the position of the core in the upstream-downstream direction is depicted in Figure 4.18-middle. Since the asymmetry is shifting the core into the upstream direction, negative values for the core bias are observed. As a function of the shower size, the core bias of the uncorrected data is constant around  $\sim -40$  m. Implementing the parametrization on the data provides a remaining core bias of about  $\pm 5$  m. Thus, the application of the derived model significantly reduces the bias. As a function of  $\sin^2\theta$ , the mean core bias decreases into negative values with growing inclination of the shower. Reaching a zenith angle of  $\sin^2\theta \approx 0.6$ , a change of slope is appearing and the core bias increases. Applying the correction results in a residual bias of  $\pm 10$  m and an approximately constant behavior as a function of  $\sin^2\theta$ . Thus, the application of the model eliminates the dependence of the core bias on the zenith angle. The core bias in the perpendicular  $x$ -direction is not shown, because the mean bias in that direction is around zero, whether the correction is applied or not.

Figure 4.18-bottom shows the resolution of the reconstruction of the core position in the shower plane as a function of the shower size and as a function of  $\sin^2\theta$ . The resolution of the core is received by computing the 68% quantile of the cumulative distribution function for the distances between the simulated and reconstructed core position. The corresponding uncertainties are calculated using the bootstrap method with 500 resamples. The core resolution decreases as a function of the shower size from  $\sim 80$  m to approximately  $\sim 50$  m.

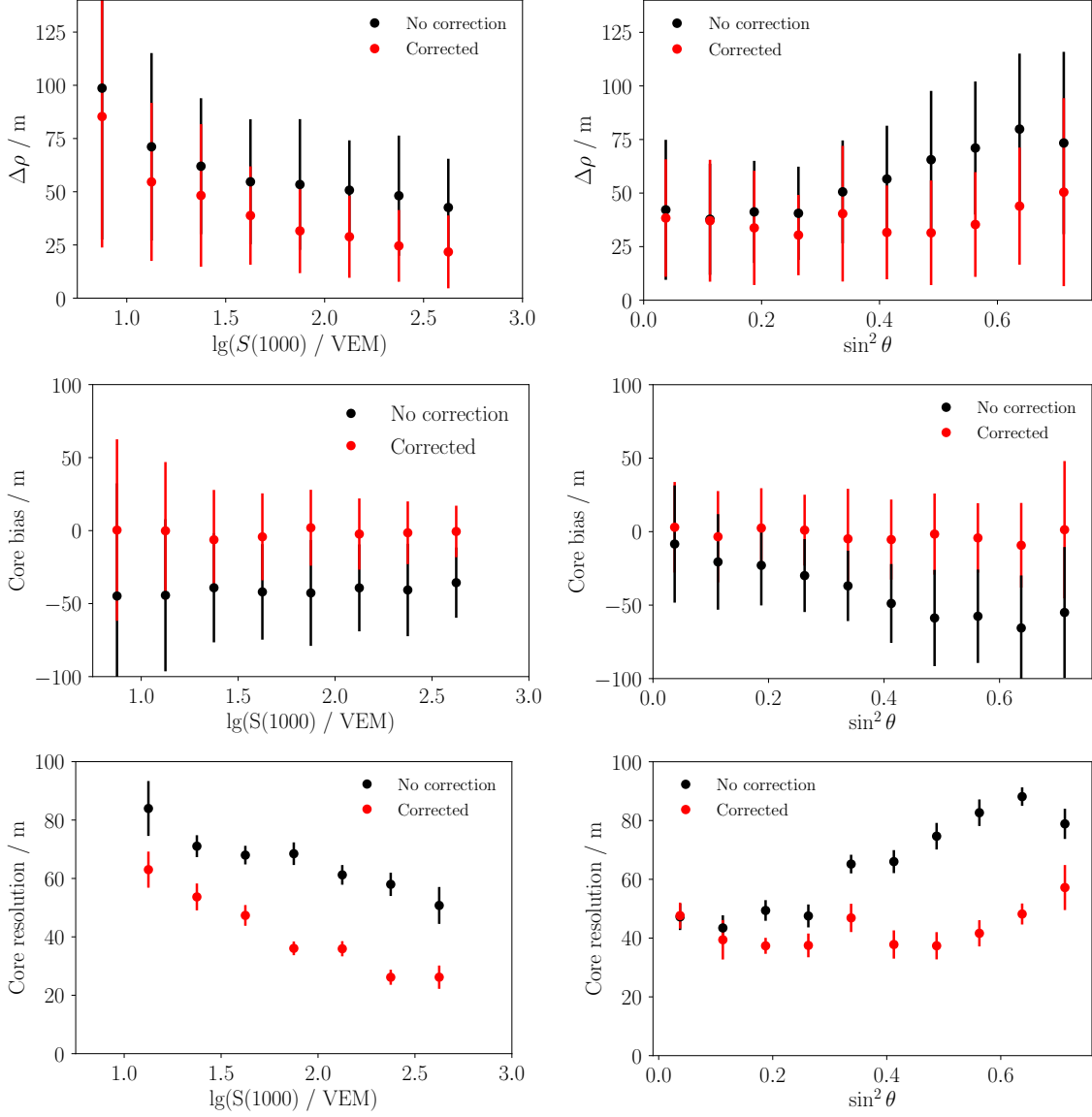


**Figure 4.18.:** *Top:* Total distance  $\Delta\rho = \sqrt{(\vec{r}_{\text{rec}} - \vec{r}_{\text{MC}})^2}$  between the reconstructed and simulated core position as a function of shower size  $\lg(S(1000)/\text{VEM})$  (*left*) and as a function of  $\sin^2\theta$  (*right*). *Middle:* Mean bias of the position of the core in the shower plane in the upstream-downstream direction as a function of shower size (*left*) and as a function of  $\sin^2\theta$  (*right*). *Bottom:* Core resolution as a function of shower size (*left*) and as a function of  $\sin^2\theta$  (*right*).

Applying the derived parametrization improves the resolution by  $\sim 20$  to  $30$  m. With increasing inclination, the core resolution increases from  $\sim 50$  m to  $\sim 90$  m. Applying the model leads to an approximately constant behavior with the inclination of the shower around the residual core resolution of  $\sim 45$  m. For highly inclined showers, from about  $\sin^2\theta \approx 0.65$ , the core resolution of the corrected data changes for the worse. Nevertheless, the application of the derived model improves the core resolution by  $\sim 20$  to  $40$  m.

On the basis of the distributions shown in Figure 4.18, it is concluded that the current correction is decreasing the bias but not completely removing it. Furthermore, it is assumed that the current model for WCDs is not impacted by the addition of a SSD on top of each WCD.

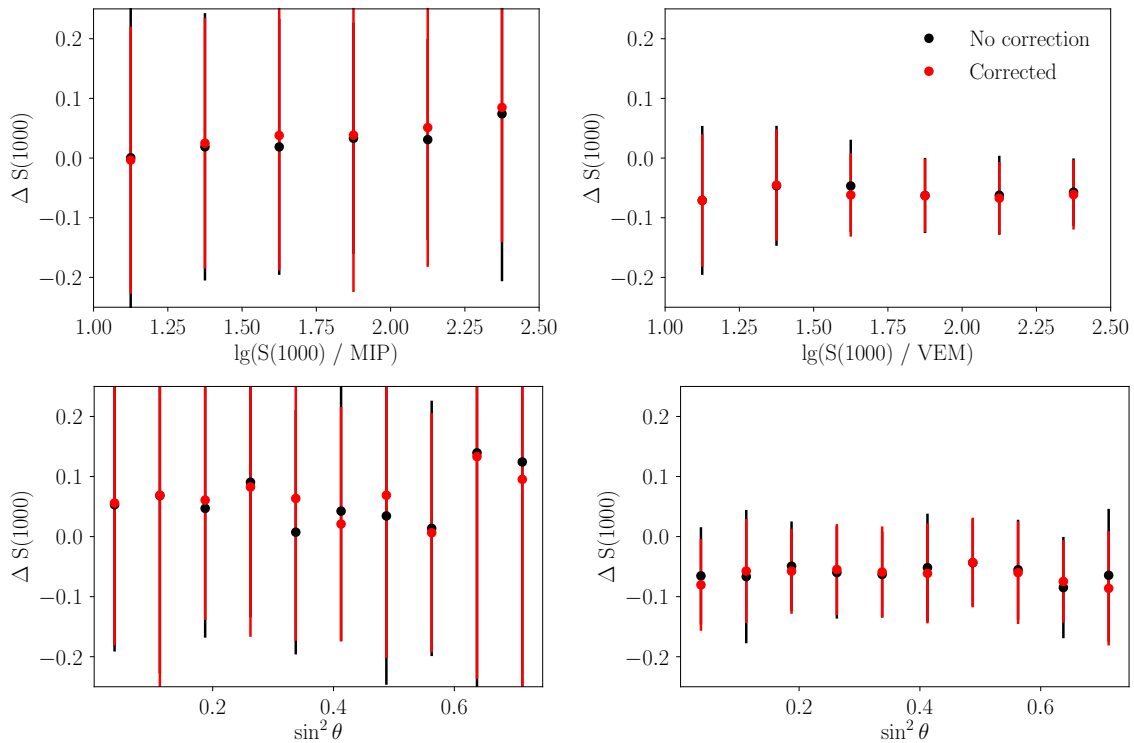


**Figure 4.19.:** Relative difference  $\Delta S(1000) = \frac{S(1000)_{\text{rec}}}{S(1000)_{\text{MC}}} - 1$  as a function of the shower size  $\lg(S(1000))$  (*top*) and as a function of  $\sin^2 \theta$  (*bottom*). *Left:* Relative difference for SSDs. *Right:* Relative difference for WCDs.

#### 4.5.2. Impact of the Asymmetry on the Shower Size

A good estimator of the shower size  $S(1000)$  can only be obtained if the position of the shower core is known with sufficient accuracy. To test, whether the asymmetry has an impact on the shower size  $S(1000)$  or not, the relative difference  $\Delta S(1000) = \frac{S(1000)_{\text{rec}}}{S(1000)_{\text{MC}}} - 1$  of the reconstructed  $S(1000)_{\text{rec}}$  and simulated shower size  $S(1000)_{\text{MC}}$  is shown for both, the corrected data and the data without correction. Examples of this distribution are shown in Figure 4.19 as a function of the energy and as a function of  $\sin^2 \theta$  for both SSDs and WCDs. The standard deviation, represented as error bars, gives the accuracy of the  $S(1000)$  reconstruction. The plots are intended to help to address the question of whether the choice of the optimal distance  $r_{\text{opt}} = 1000$  m minimizes fluctuations due to asymmetries. For WCDs, the asymmetry as a function of the distance is flat around  $r = 1000$  m. Thus, it is assumed that the correction does not impact  $S(1000)$ . For SSDs, the asymmetry increases with distance and therefore is not flat around  $r = 1000$  m.

However, contrary to expectation, after applying the correction, no impact on  $S(1000)$  or their uncertainties is observed for either detector. It is also noticeable, that the uncertainties for SSDs are significantly larger than the uncertainties for WCDs. This observed behavior is still under investigation. Looking at the plots for WCDs, it is conspicuous that the values for  $\Delta S(1000)$  are centered around  $\sim -0.08$ , while the values for SSDs are centered around  $\sim 0.05$ . The origin of this observed bias for WCDs is unclear. It seems that this bias is not caused by the asymmetry, so other effects could be involved to explain the bias.

#### 4.5.3. Comparison with Existing Model

Since a model correcting the azimuthal asymmetry in signals already exists for WCDs in [1], the model derived in this thesis is compared to it. The parametrization of the asymmetry for the current model in WCDs, without taking energy dependency into account, is expressed

**Table 4.5.:** Fit parameters for WCDs averaged over all energies in comparison with the old model.

Fit parameter	WCD	
	New model	Old model
$a_0$	0.0219	Fixed to 0
$a_1$	0.423	0.455
$a_2$	0.733	0.737
$a_3$	-0.0812	-0.068
$b_1/m$	-988	-611
$b_2/m$	931	524

as

$$\alpha(r, \theta) = a(\theta) \operatorname{erf} \left( \frac{r}{b(\theta)} \right), \quad (4.20)$$

with

$$a(\theta) = \frac{a_0 + a_1 \sin^2 \theta}{\left( 1 + \exp \left( -\frac{\sin^2 \theta - a_2}{a_3} \right) \right)}, \quad (4.21)$$

and

$$b(\theta) = b_1 \sin^4 \theta + b_2. \quad (4.22)$$

The corresponding fit parameters are listed in Table 4.5 with the fit parameters of the new derived model next to them for better comparability. Figure 4.20-left illustrates the fit parameter  $a(\theta)$  as a function of  $\sin^2 \theta$  for the new and the old model in comparison. Both models use the same fit function and have really similar results. The only difference is the slightly steeper slope of the old model.

Figure 4.20-right depicts the fit parameter  $b(\theta)$  as a function of  $\sin^2 \theta$  for the new model and the old model. The two models differ mainly in the derived model function to fit  $b(\theta)$ . The old model uses a second order polynomial, while the new model uses a first order polynomial instead. Despite their different fit functions, the two models are compatible within their uncertainties. The good agreement of the current model with the new model for WCDs, validates the new model for WCDs and, by extension, reinforces the obtained model for SSDs.

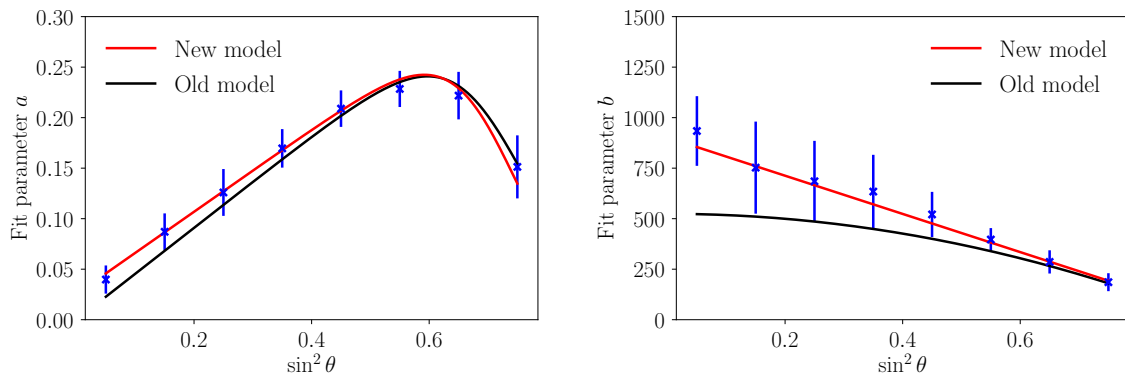


**Figure 4.20.:** Comparison of the old model (black) with the new model (red) for WCDs. The data points are averaged over all energies, with the standard deviation as error bars. *Left:* Fit parameter  $a(\theta)$  as a function of  $\sin^2 \theta$ . *Right:* Fit parameter  $b(\theta)$  as a function of  $\sin^2 \theta$ .

## 5. Conclusion and Outlook

This research aimed to study the evolution of the azimuthal asymmetry as a function of the energy and zenith angle of the CR and of the distance from the shower axis in WCDs and SSDs. Based on this analysis, a parametrization for correcting the bias in the position of the shower core is derived.

It has been shown that an azimuthal asymmetry of the signals occurs in inclined showers, due to a combination of geometrical and attenuation effects. The impact of the geometrical effect is dominant at small distances. For large distances, a combination of both asymmetry causing effects needs to be considered.

The two considered detectors, WCD and SSD, emphasize different shower components depending on the distance, leading to different amplitudes of the asymmetry. The SSD is mainly driven by the electromagnetic shower component for all distances from the shower axis. For the WCD, the contribution of the components to the total signal is more complex and depends strongly on the distance. Near the shower axis, the electromagnetic component dominates, while at long distances the muonic component mainly drives the total signals. These different detector responses result in a larger amplitude of asymmetry for SSDs at large distances, in contrast to WCDs.

In addition, it has been shown that at small zenith angles, the impact of the geometric effect dominates, resulting in an increase of the amplitude. Above a certain inclination of  $\sin^2 \theta \approx 0.6$ , the shower is dominated by muons, due to the progressive attenuation of the electromagnetic component, leading to a decrease in the amplitude of the asymmetry. Comparing the plots of the amplitude of asymmetry for different energies, it is assumed that energy dependence is a second order effect, since the plots are compatible within their respective errors.

Not taking the observed asymmetry in signals into account, introduces a bias in the position of the reconstructed shower core of about  $\sim 40$  m in the upstream direction. For a shower with an inclination of  $\sin^2 \theta \approx 0.6$ , the mean core bias increases up to  $\sim 70$  to  $80$  m. Applying the derived model reduces this bias in the position of the core to an residual bias of less than  $\pm 10$  m. In addition, the core resolution is improved by  $\sim 20$  to  $40$  m, depending on the energy and zenith angle of the CR. The observations have shown that the WCDs are not affected by the placement of SSDs on top. Since the reconstruction of the core position using SSD data has not yet been developed, the derived model for SSDs can not be tested in this thesis. Nevertheless, the good agreement of the current model with the new model for WCDs, reinforces the derived model for SSDs.

Since the bias is not completely eliminated, the derived model should be further improved in future researches. In future work, the study of a larger number of simulated events may prove important. This would also allow the energy dependence to be taken into account. In addition, although the reconstruction of the shower core is assumed to be driven by the closest detectors, the model can be further developed by considering the decrease of the amplitude for WCDs at large distances. Future studies may also find better fit parameters, where the fit functions goes through the origin, as expected. With such values in the

developed models, no asymmetry would appear for vertically incident air showers.

Also, for the plots of the relative difference  $\Delta S(1000)$  as a function of the energy and zenith angle, many questions remain unanswered, that should be investigated in future studies. For example the large uncertainties and the missing impact of the correction for SSDs or the observed bias for WCDs should be examined in more details.

It is a question of future research to develop the reconstruction of the core position using SSD data. If the position of the shower core is reconstructed in two different ways, using data from two independent detectors, the accuracy of the position is significantly improved. Once the reconstruction of the core position for SSD data has been developed, the model for SSDs, derived in this thesis, can be applied. With regard to the good agreement of the old and the new WCD model and all the tests performed in this thesis, it is assumed that applying the model for SSDs reduces the bias in the position of the core and improves its core resolution in a similar way as the model for WCDs.

# Appendix

## A. Fit Parameters Dependency on Distance

**Table A.1.:** Fitting parameters of  $a(\theta)$  in each energy range for WCDs.

WCD Fit parameters of $a(\theta)$									
$\lg(E/\text{eV})$	$a_0$	Error $a_0$	$a_1$	Error $a_1$	$a_2$	Error $a_2$	$a_3$	Error $a_3$	
18.5	18.6	0.00916	0.0174	0.386	0.0494	0.713	0.0264	-0.0391	0.0239
18.6	18.7	0.0395	0.0360	0.331	0.111	0.725	0.0404	-0.0657	0.0418
18.7	18.8	0.0149	0.0338	0.391	0.0948	0.713	0.0187	-0.0527	0.0141
18.8	18.9	0.0226	0.0150	0.395	0.0819	0.716	0.0406	-0.0883	0.0398
18.9	19.0	-0.0104	0.0201	0.439	0.0794	0.729	0.0407	-0.0955	0.0493
19.0	19.1	0.0364	0.0231	0.312	0.0632	0.755	0.0176	-0.0360	0.0407
19.1	19.2	0.00899	0.0230	0.476	0.120	0.749	0.0568	-0.126	0.0633
19.2	19.3	0.0275	0.0195	0.444	0.121	0.723	0.0497	-0.106	0.0666
19.3	19.4	0.0151	0.0163	0.381	0.0460	0.751	0.0126	-0.0304	0.0191
19.4	19.5	-0.00554	0.0114	0.530	0.0963	0.741	0.0444	-0.117	0.0649
19.5	19.6	0.0269	0.0195	0.507	0.106	0.725	0.0403	-0.118	0.0509
19.6	19.7	0.049	0.0222	0.359	0.0762	0.774	0.0241	-0.0828	0.0476
19.7	19.8	0.0218	0.0189	0.496	0.0758	0.712	0.0247	-0.0933	0.0271
19.8	19.9	0.0502	0.0209	0.416	0.0954	0.722	0.0302	-0.0851	0.0340
19.9	20.0	0.0222	0.0203	0.478	0.0942	0.754	0.0247	-0.0811	0.0479

**Table A.2.:** Fitting parameters of  $b(\theta)$  in each energy range for WCDs.

WCD Fit parameters of $b(\theta)$					
$\lg(E_{\min}/\text{eV})$	$\lg(E_{\max}/\text{eV})$	$b_1/\text{m}$	Error $b_1/\text{m}$	$b_2/\text{m}$	Error $b_2/\text{m}$
18.5	18.6	-369	391	519	198
18.6	18.7	-766	387	738	196
18.7	18.8	-778	248	725	155
18.8	18.9	-727	356	743	188
18.9	19.0	-464	430	555	229
19.0	19.1	-694	433	733	241
19.1	19.2	-1160	425	1010	264
19.2	19.3	-987	397	929	213
19.3	19.4	-686	311	769	195
19.4	19.5	-888	387	904	210
19.5	19.6	-1660	478	1360	236
19.6	19.7	-1170	385	1080	226
19.7	19.8	-1560	749	1310	410
19.8	19.9	-1670	369	1410	185
19.9	20.0	-1240	415	1170	214

**Table A.3.:** Fitting parameters of  $a(\theta)$  in each energy range for SSDs.

SSD Fit parameters of $a(\theta)$									
$\lg(E/\text{eV})$	$a_0$	Error $a_0$	$a_1$	Error $a_1$	$a_2$	Error $a_2$	$a_3$	Error $a_3$	
18.5	18.6	24.1	9.28	-31.0	7.59	0.974	0.120	0.150	0.0286
18.6	18.7	15.0	8.66	-19.3	0.573	0.844	0.0472	0.135	0.0104
18.7	18.8	15.0	6.56	-18.9	0.411	1.06	0.0629	0.218	0.0204
18.8	18.9	15.0	7.77	-19.0	0.398	0.890	0.0476	0.145	0.0114
18.9	19.0	15.0	6.21	-19.4	0.422	0.842	0.0385	0.144	0.00991
19.0	19.1	15.0	8.79	-18.4	0.669	0.988	0.0559	0.176	0.0134
19.1	19.2	19.2	2.00	-23.2	2.54	1.06	0.0726	0.180	0.0168
19.2	19.3	19.3	3.37	-23.4	4.60	1.01	0.0825	0.172	0.0166
19.3	19.4	24.8	9.18	-29.8	3.96	1.09	0.0561	0.179	0.0125
19.4	19.5	15.0	9.12	-18.0	0.563	0.982	0.0463	0.177	0.0121
19.5	19.6	15.0	8.03	-18.3	0.695	0.947	0.0532	0.168	0.0128
19.6	19.7	19.3	1.45	-23.1	1.81	1.05	0.0613	0.185	0.0144
19.7	19.8	15.0	8.06	-18.2	0.834	0.923	0.0357	0.161	0.0100
19.8	19.9	19.2	2.04	-23.1	2.61	1.02	0.0380	0.177	0.00863
19.9	20.0	23.9	9.43	-28.8	9.50	1.07	0.0802	0.183	0.0119

**Table A.4.:** Fitting parameters of  $b(\theta)$  in each energy range for SSDs.

SSD Fit parameters of $b(\theta)$					
$\lg(E_{\min}/\text{eV})$	$\lg(E_{\max}/\text{eV})$	$b_1/\text{m}$	Error $b_1/\text{m}$	$b_2/\text{m}$	Error $b_2/\text{m}$
18.5	18.6	-694	823	911	376
18.6	18.7	-280	750	696	386
18.7	18.8	-1630	564	1380	378
18.8	18.9	-617	461	770	263
18.9	19.0	-430	406	820	176
19.0	19.1	-782	554	914	342
19.1	19.2	-1120	632	1190	367
19.2	19.3	-953	571	1100	342
19.3	19.4	-935	532	1090	344
19.4	19.5	-763	710	1020	393
19.5	19.6	-392	660	846	360
19.6	19.7	-1340	611	1460	284
19.7	19.8	-878	618	1300	223
19.8	19.9	-1250	728	1570	429
19.9	20.0	-536	420	1140	161

## B. Fit Parameters Dependency on Zenith Angle

**Table B.5.:** Fitting parameters of  $c(r)$  in each energy range for WCDs.

WCD Fit parameters of $c(r)$					
$\lg(E_{\min}/\text{eV})$	$\lg(E_{\max}/\text{eV})$	$c_1/\text{m}^{-1}$	Error $c_1/\text{m}^{-1}$	$c_2$	Error $c_2$
18.5	18.6	-3.63e-06	3.58e-05	-0.00583	0.0152
18.6	18.7	4.66e-05	3.15e-05	-0.0138	0.0145
18.7	18.8	3.99e-05	3.94e-05	-0.0169	0.0182
18.8	18.9	4.50e-05	2.38e-05	-0.0173	0.0128
18.9	19.0	8.06e-05	3.41e-05	-0.0312	0.0180
19.0	19.1	2.88e-05	2.96e-05	-0.0133	0.0170
19.1	19.2	2.53e-05	2.56e-05	-0.0180	0.0136
19.2	19.3	3.64e-05	2.01e-05	-0.0190	0.0121
19.3	19.4	1.53e-05	2.03e-05	-0.0173	0.0121
19.4	19.5	5.82e-06	1.40e-05	-0.0102	0.00928
19.5	19.6	2.95e-05	1.41e-05	-0.0130	0.0101
19.6	19.7	5.16e-05	1.91e-05	-0.0268	0.0168
19.7	19.8	3.11e-05	1.63e-05	-0.0303	0.0145
19.8	19.9	4.35e-05	1.54e-05	-0.0191	0.0149
19.9	20.0	3.86e-05	1.46e-05	-0.022	0.0144

**Table B.6.:** Fitting parameters of  $d(r)$  in each energy range for WCDs.

WCD Fit parameters $d(r)$					
$\lg(E_{\min}/\text{eV})$	$\lg(E_{\max}/\text{eV})$	$d_1$	Error $d_1$	$d_2/\text{m}$	Error $d_2/\text{m}$
18.5	18.6	0.433	0.0432	348	82.8
18.6	18.7	0.348	0.0408	263	94.5
18.7	18.8	0.371	0.0447	275	90.1
18.8	18.9	0.395	0.0463	365	104
18.9	19.0	0.356	0.0448	254	109
19.0	19.1	0.371	0.0453	308	107
19.1	19.2	0.399	0.0496	333	107
19.2	19.3	0.395	0.0400	338	108
19.3	19.4	0.450	0.0325	346	61.1
19.4	19.5	0.458	0.0360	460	87.8
19.5	19.6	0.409	0.0424	408	114
19.6	19.7	0.367	0.0356	299	101
19.7	19.8	0.459	0.0381	429	101
19.8	19.9	0.391	0.0363	396	129
19.9	20.0	0.417	0.0376	368	108

**Table B.7.:** Fitting parameters of  $e(r)$  in each energy range for WCDs.

WCD Fit parameters of $e(r)$					
$\lg(E_{\min}/\text{eV})$	$\lg(E_{\max}/\text{eV})$	$e_1/\text{m}^{-1}$	Error $e_1/\text{m}^{-1}$	$e_2$	Error $e_2$
18.5	18.6	-9.53e-05	5.74e-05	0.753	0.0340
18.6	18.7	-1.14e-04	6.61e-05	0.791	0.0444
18.7	18.8	1.26e-06	4.27e-05	0.731	0.0215
18.8	18.9	-1.42e-04	6.90e-05	0.815	0.0462
18.9	19.0	-6.98e-05	7.11e-05	0.783	0.0554
19.0	19.1	-5.50e-05	4.07e-05	0.792	0.0380
19.1	19.2	-9.77e-05	5.70e-05	0.839	0.0505
19.2	19.3	-1.10e-04	4.46e-05	0.826	0.0466
19.3	19.4	-6.13e-05	2.66e-05	0.812	0.0308
19.4	19.5	-7.05e-05	3.10e-05	0.822	0.0407
19.5	19.6	-4.67e-05	3.00e-05	0.811	0.0404
19.6	19.7	-5.17e-05	2.67e-05	0.809	0.0281
19.7	19.8	-4.66e-05	2.76e-05	0.794	0.0374
19.8	19.9	-3.25e-05	1.80e-05	0.778	0.0251
19.9	20.0	-2.85e-05	2.78e-05	0.799	0.0433

**Table B.8.:** Fitting parameters of  $d(r)$  in each energy range for SSDs.

SSD Fit parameters $d(r)$					
$\lg(E_{\min}/\text{eV})$	$\lg(E_{\max}/\text{eV})$	$d_1/\text{m}^{-1}$	Error $d_1/\text{m}^{-1}$	$d_2$	Error $d_2$
18.5	18.6	-0.000290	0.00345	-23.7	1.58
18.6	18.7	-0.00181	0.00314	-22.5	1.75
18.7	18.8	-0.00552	0.00129	-22.5	0.723
18.8	18.9	-0.00368	0.00252	-21.2	1.57
18.9	19.0	-0.00275	0.00253	-22.1	1.71
19.0	19.1	-0.00145	0.00235	-22.5	1.53
19.1	19.2	-0.00327	0.00209	-20.3	1.43
19.2	19.3	-0.00409	0.00180	-20.4	1.49
19.3	19.4	-0.00195	0.00150	-21.5	1.22
19.4	19.5	-0.00241	0.00135	-20.9	1.27
19.5	19.6	-0.00157	0.00142	-21.6	1.42
19.6	19.7	-0.00321	0.00117	-20.2	1.03
19.7	19.8	-0.00369	0.00139	-19.6	1.55
19.8	19.9	-0.00127	0.000670	-22.2	0.784
19.9	20.0	-0.00135	0.000763	-21.9	1.05

**Table B.9.:** Fitting parameters of  $e(r)$  in each energy range for SSDs.

SSD Fit parameters $e(r)$							
$\lg(E/\text{eV})$		$e_1/\text{m}^{-2}$	Error $e_1/\text{m}^{-2}$	$e_2/\text{m}^{-1}$	Error $e_2/\text{m}^{-1}$	$e_3$	Error $e_3$
18.5	18.6	7.54e-07	3.21e-07	-0.00103	0.000317	1.42	0.0722
18.6	18.7	2.21e-07	1.92e-07	-0.000518	0.000227	1.32	0.0615
18.7	18.8	3.48e-07	1.42e-07	-0.000714	0.000165	1.37	0.0431
18.8	18.9	2.29e-07	1.77e-07	-0.000518	0.000210	1.34	0.0558
18.9	19.0	5.14e-07	1.47e-07	-0.000861	0.000185	1.40	0.0548
19.0	19.1	4.10e-07	1.77e-07	-0.000712	0.000219	1.37	0.0619
19.1	19.2	4.91e-07	1.79e-07	-0.000824	0.000222	1.43	0.0633
19.2	19.3	2.08e-07	1.02e-07	-0.000517	0.000151	1.34	0.0516
19.3	19.4	2.61e-07	9.70e-08	-0.000569	0.000145	1.36	0.0503
19.4	19.5	5.21e-08	5.94e-08	-0.000283	0.000103	1.28	0.0403
19.5	19.6	2.01e-07	6.49e-08	-0.000495	0.000112	1.35	0.0441
19.6	19.7	1.25e-07	5.86e-08	-0.000397	0.000101	1.33	0.0400
19.7	19.8	1.37e-07	4.20e-08	-0.000458	8.01e-05	1.37	0.0363
19.8	19.9	4.13e-08	3.00e-08	-0.000238	6.57e-05	1.26	0.0324
19.9	20.0	8.2e-08	3.01e-08	-0.000312	6.67e-05	1.29	0.0319



# Acknowledgements

First, I would like to thank Prof. Dr. Ralph Engel and Dr. Markus Roth for being the reviewers of this thesis and for enabling me to write my thesis at the Institute for Astroparticle Physics.

My greatest thanks go to my supervisor, Dr. Quentin Luce, who advised and guided me throughout the thesis. He supported me with his knowledge and ideas, gave me useful feedback and proofread this thesis.

Finally, I thank my family and friends who supported me during this time and additionally proofread this thesis.



# Bibliography

- [1] Q. Luce, M. Roth, D. Schmidt, and D. Veberic. On the need for unbiasing azimuthal asymmetries in signals measured by surface detector arrays. *PoS, ICRC2021:435*, 2021.
- [2] *Nuclear Instruments and Methods in Physics Research Section A: Accelerators, Spectrometers, Detectors and Associated Equipment*, 798:172–213, Oct 2015.
- [3] A timeline of high-energy cosmic rays history. <https://www.auger.org/outreach/cosmic-rays/timeline-cosmic-rays>. Accessed: 2022-01-25.
- [4] M. S. Potgieter. Solar Modulation of Cosmic Rays. *Living Reviews in Solar Physics*, June 2013.
- [5] A. Aab et al. Measurement of the cosmic-ray energy spectrum above  $2.5 \times 10^{18}$  eV using the pierre auger observatory. *Physical Review D*, 102(6), Sep 2020.
- [6] F. E. Taylor. Comparison of cosmic ray flux at  $\sqrt{s} \geq 14$  TeV with LHC luminosity. 5 2008.
- [7] Theodor wulf a new electrometer and the eiffel tower. <https://timeline.web.cern.ch/theodor-wulf-new-electrometer-and-eiffel-tower>. Accessed: 2022-01-26.
- [8] T. Wulf. Über die in der Atmosphäre vorhandene Strahlung von hoher Durchdringungsfähigkeit. *Physikalische Zeitschrift*, 10:152–157, 1909.
- [9] V. F. Hess. Über Beobachtungen der durchdringenden Strahlung bei sieben Freiballonfahrten. *Phys. Z.*, 13:1084–1091, 1912.
- [10] Cosmic rays discovered 100 years ago. <https://home.cern/news/news/physics/cosmic-rays-discovered-100-years-ago>. Accessed: 2022-01-26.
- [11] S. P. Swordy. The Energy Spectra and Anisotropies of Cosmic Rays. , 99:85–94, October 2001.
- [12] V. Verzi. Cosmic rays: air showers from low to high energies: Rapporteur Report. *PoS, ICRC2015:015*, 2016.
- [13] A. M. Hillas. Cosmic Rays: Recent Progress and some Current Questions. *arXiv e-prints*, pages astro-ph/0607109, July 2006.
- [14] K. A. Eriksen et al. Evidence for particle acceleration to the knee of the cosmic ray spectrum in tycho’s supernova remnant. *The Astrophysical Journal*, 728(2):L28, Jan 2011.
- [15] T. Antoni et al. Cascade measurements of energy spectra for elemental groups of cosmic rays: Results and open problems. *Astroparticle Physics*, 24(1):1–25, 2005.
- [16] K. Greisen. End to the Cosmic-Ray Spectrum? *Physical Review Letters*, 16:748–750, April 1966.

- [17] G. T. Zatsepin and V. A. Kuz'min. Upper Limit of the Spectrum of Cosmic Rays. *Soviet Journal of Experimental and Theoretical Physics Letters*, 4:78, August 1966.
- [18] J. Bellido for the Pierre Auger Collaboration. Depth of maximum of air-shower profiles at the Pierre Auger Observatory: Measurements above  $10^{17.2}$  eV and Composition Implications. In *35th International Cosmic Ray Conference (ICRC 2017)*.
- [19] Cosmic rays: particles from outer space. <https://home.cern/science/physics/cosmic-rays-particles-outer-space>. Accessed: 2021-12-20.
- [20] K. Kotera and A. V. Olinto. The astrophysics of ultrahigh-energy cosmic rays. *Annual Review of Astronomy and Astrophysics*, 49(1):119–153, Sep 2011.
- [21] A. Aab et al. Observation of a large-scale anisotropy in the arrival directions of cosmic rays above  $8 \times 10^{18}$  eV. *Science*, 357(6357):1266–1270, Sep 2017.
- [22] M. Bustamante et al. High-energy cosmic-ray acceleration. *2009 CERN - Latin-American School of High-Energy Physics*, pp.533-540.
- [23] A. Bridgeman. *Determining the Mass Composition of Ultra-high Energy Cosmic Rays Using Air Shower Universality*. PhD thesis, Karlsruhe, 2018.
- [24] P. Auger, R. Maze, and T. Grivet-Mayer. Grandes gerbes cosmiques atmosphériques contenant des corpuscules ultrapénétrants. *Compt. Rend. Hebd. Seances Acad. Sci.*, 206(23):1721–1723, 1938.
- [25] K. Kampert and A. A. Watson. Extensive air showers and ultra high-energy cosmic rays: a historical review. *The European Physical Journal H*, 37(3):359–412, Jul 2012.
- [26] A. Zilles. *Emission of Radio Waves in Particle Showers: Validation of microscopic simulations with the SLAC T-510 experiment and their potential in the future Square Kilometre Array*. Springer, 2017.
- [27] J. Matthews. A heitler model of extensive air showers. *Astroparticle Physics*, 22(5):387–397, 2005.
- [28] I. Valiño, J. Alvarez-Muñiz, M. Roth, R.A. Vazquez, and E. Zas. Characterisation of the electromagnetic component in ultra-high energy inclined air showers. *Astroparticle Physics*, 32(6):304–317, Jan 2010.
- [29] J. Matthews et al. A parameterization of cosmic ray shower profiles based on shower width. *Journal of Physics G: Nuclear and Particle Physics*, 37(2):025202, Jan 2010.
- [30] Pierre auger observatory, photo galleries (flickr). <https://www.flickr.com/photos/134252569@N07/albums/72157659225375559/with/22089748836/>. Accessed: 2021-12-07.
- [31] M. T. Dova. Ultra-High Energy Cosmic Rays. In *7th CERN Latin-American School of High-Energy Physics*, pages 169–190, 2015.
- [32] D. Gora. The Pierre Auger Observatory: review of latest results and perspectives. *Universe*, 4(11):128, 2018.
- [33] A. A. Watson. The discovery of cherenkov radiation and its use in the detection of extensive air showers. *Nuclear Physics B - Proceedings Supplements*, 212-213:13–19, Mar 2011.
- [34] X. Bertou et al. Calibration of the surface array of the Pierre Auger Observatory. *Nucl. Instrum. Meth. A*, 568:839–846, 2006.

- 
- [35] A. Aab et al. Reconstruction of events recorded with the surface detector of the Pierre Auger Observatory. *JINST*, 15(10):P10021, 2020.
- [36] A hybrid detector. <https://www.auger.org/index.php/observatory/auger-hybrid-detector>. Accessed: 2021-12-07.
- [37] D. Schmidt. The scintillator upgrade detectors of the auger observatory, HIRSAP workshop 2019. <https://indico.scc.kit.edu/event/559/contributions/6073/>, 2019. Accessed: 2022-02-05.
- [38] A. Aab et al. The Pierre Auger Observatory Upgrade - Preliminary Design Report. 4 2016.
- [39] A. Aab et al. Observation of inclined EeV air showers with the radio detector of the pierre auger observatory. *Journal of Cosmology and Astroparticle Physics*, 2018(10):026–026, Oct 2018.
- [40] D. Schmidt. Scintillator Surface Detector simulations for AugerPrime. *EPJ Web Conf.*, 210:06010, 2019.
- [41] ROOT data analysis framework. <https://root.cern/>. Accessed: 2021-09-01.
- [42] S. Argiro et al. The Offline Software Framework of the Pierre Auger Observatory. *Nucl. Instrum. Meth. A*, 580:1485–1496, 2007.
- [43] T. Pierog et al. EPOS LHC: Test of collective hadronization with data measured at the CERN Large Hadron Collider. *Phys. Rev. C*, 92:034906, Sep 2015.
- [44] C. Pryke. Asymmetry of Air Showers at Ground Level. *GAP1998-034*.
- [45] P. Billoir, P. Da Silva, and X. Bertou. Checking the Origin of the Asymmetry of the Surface Detector Signals. *GAP2002-074*.
- [46] iminuit. <https://iminuit.readthedocs.io/en/stable/>. Accessed: 2021-12-06.
- [47] D. Schmidt for the Pierre Auger Collaboration. Reconstruction of events recorded with the water-cherenkov and scintillator surface detectors of the pierre auger observatory. Lecture held at 37th International Cosmic Ray Conference (ICRC 2021).
- [48] L. Armbruster. Asymmetries of the Lateral Distribution of Particles at the Ground, bachelor thesis, KIT, 2018.
- [49] M. Münchmeyer and A. Letessier-Selvon. Effects of the geomagnetic field on energy estimation and large-scale anisotropy search. *GAP2010-028*.